

VOLATILE-RICH EVOLUTION OF MOLTEN SUPER-EARTH L 98-59 D

PREPRINT, COMPILED JULY 4, 2025

Harrison Nicholls¹, Tim Lichtenberg², Richard D. Chatterjee¹, Claire Marie Guimond¹, Emma Postolec², and Raymond T. Pierrehumbert¹

¹Department of Physics, University of Oxford, United Kingdom

²Kapteyn Astronomical Institute, University of Groningen, The Netherlands

ABSTRACT

Small low-density exoplanets are sculpted by strong stellar irradiation but their origin is unknown. Two competing (Valencia et al., 2025; Zeng et al., 2019) scenarios are that they formed either with rocky interiors and H₂-He atmospheres (‘gas-dwarfs’; e.g. Rogers et al. (2023); Owen and Wu (2017)), or instead with bulk compositions dominated by H₂O phases (‘water-worlds’; e.g. Luque and Palle (2022); Burn et al. (2024)). Observations of L 98-59 d have revealed its unusually low density and spectral characteristics (Banerjee et al., 2024; Gressier et al., 2024), opening a window for disentangling its origin (Pass et al., 2025). We constrain the possible range of evolutionary histories linking L 98-59 d’s birth conditions to these observations, using a coupled atmosphere-interior modelling framework (Lichtenberg et al., 2021; Nicholls et al., 2024a, 2025a). Observations are explained by a chemically-reducing mantle and early substantial (>1.8 mass%) sulfur and hydrogen content, inconsistent with both the gas-dwarf and water-world origin scenarios. Observed spectral features are explained by in-situ photochemical production of SO₂ in an H₂ background (Tsai et al., 2023). L 98-59 d’s interior comprises a permanent magma ocean, allowing long-term retention of volatiles within its interior (Dorn and Lichtenberg, 2021; Shorttle et al., 2024) over billions of years, consistent with surveyed Kepler Survey trends (David et al., 2021). Modelling of the ‘cosmic shoreline’ suggests (Ji et al., 2025) that early volatile-metal budget is a determinant of atmospheric retention - here, we explicitly show that large initial budgets can explain JWST observations of some super-Earth planets (including DDT targets). In breaking with the supposed gas-dwarf/water-world dichotomy, we reveal an evolutionary pathway defined by high-molar-mass atmospheres overlying magma oceans, and invite a more nuanced taxonomy of small exoplanets.

Keywords exoplanet, super-Earth, magma, redox, chemistry, atmosphere, jwst, escape, volatile, inventory

1 MAIN TEXT

The super-Earth (radii $\lesssim 1.7R_{\oplus}$) and sub-Neptune (radii $\sim 1.7 - 4R_{\oplus}$) exoplanet populations have no Solar-System analogues but are amenable to spectroscopic characterisation with current instruments (Kempton and Knutson, 2024; Lichtenberg and Miguel, 2025). Surveys indicate a dearth of planets with radii between the two regimes: the radius valley (Fulton and Petigura, 2018; David et al., 2021). It remains unclear how these proposed classes originate and if their formation is related. Two competing scenarios are often considered (Valencia et al., 2025; Zeng et al., 2019): they may form jointly as *gas-dwarfs* with large envelopes (primarily H₂-He) that eventually diverge due to long-term atmospheric escape processes (Owen, 2019; Lopez, 2017), or they could be *water-worlds* that differ by H₂O content from formation (Mousis et al., 2020; Luque and Palle, 2022; Lacedelli et al., 2022; Burn et al., 2024). An apparent over-abundance of young sub-Neptune planets may represent a reservoir of future super-Earths, which if true, intimately links these proposed populations across the radius valley (Fernandes et al., 2025; David et al., 2021).

L 98-59 hosts three transiting exoplanets (Demangeon et al., 2021). HST observations of the innermost planet (mass $0.47M_{\oplus}$, radius $0.85R_{\oplus}$) rule out a low mean-molecular-weight (MMW) primary atmosphere Zhou et al. (2022), but recent JWST transit spectroscopy has indicated an SO₂-rich atmosphere (Bello-Arufe et al., 2025). HST observations of the outermost transiting planet (L 98-59 d) have also ruled out a pure H₂-He atmosphere (Zhou et al., 2023). Yet L 98-59 d’s low bulk-density (3.45 g cm^{-3} , mass $2.14M_{\oplus}$, radius $1.52R_{\oplus}$) is inconsistent with a pure rock-and-iron composition, but consistent with it hosting atmosphere-forming volatiles in a gaseous envelope (Rajpaul et al., 2024; Demangeon

et al., 2021). Sitting on the edge of the radius valley, this planet stands out among the low-mass population as a prime case for tracing the physics of rocky planet formation and evolution (Parc et al., 2024). Retrievals on its transit spectrum point to an atmosphere of sulfur-bearing volatiles (H₂S, SO₂) within a background of H₂. Free-chemistry models fit at 5.6σ with a MMW of $9.18^{+2.51}_{-2.41} \text{ g mol}^{-1}$ and an H₂S volume mixing ratio of $10^{-0.74^{+0.14}_{-0.49}}$ (Gressier et al., 2024). However, thermochemical equilibrium models fit with a MMW of $32.13^{+1.50}_{-8.31} \text{ g mol}^{-1}$ at a lower significance of only 2.7σ . Retrievals also place weak constraints on H₂O, CO₂, and CH₄ (Banerjee et al., 2024).

Here, we constrain the plausible set of evolutionary pathways linking L 98-59 d’s birth conditions to these observations. We use the PROTEUS modelling framework to create a grid of self-consistent fully-coupled atmosphere-interior evolutionary simulations (Lichtenberg et al., 2021; Nicholls et al., 2024b,a, 2025a). PROTEUS calculates the evolving thermochemical state of the planet’s interior and atmosphere over time. From a molten-start, we account for bottom-up mantle crystallisation, tidal dissipation, outgassing and escape of CHNOS volatiles, atmospheric blanketing and energy transport, and stellar evolution. Our radiative-convective atmosphere implements a real-gas equation-of-state, correlated-*k* radiative transfer, and allows the formation of deep radiative layers (Innes et al., 2023; Nicholls et al., 2024a). Stellar XUV fluxes are used to calculate the rate of volatile loss (see Methods) using an energy-limited hydrodynamic escape parametrisation (Lehmer and Catling, 2017). Our main grid of 900 models has four axes: initial volatile endowment (proxied as hydrogen atoms relative to the mantle (melt + solid) mass, $1000 \leq H_{\text{ppmw}} \leq 16000$), bulk S/H mass ratio, magma ocean oxygen fugacity, and total planet mass (Rajpaul et al., 2024). The grid domain spans expected post-accretion sce-

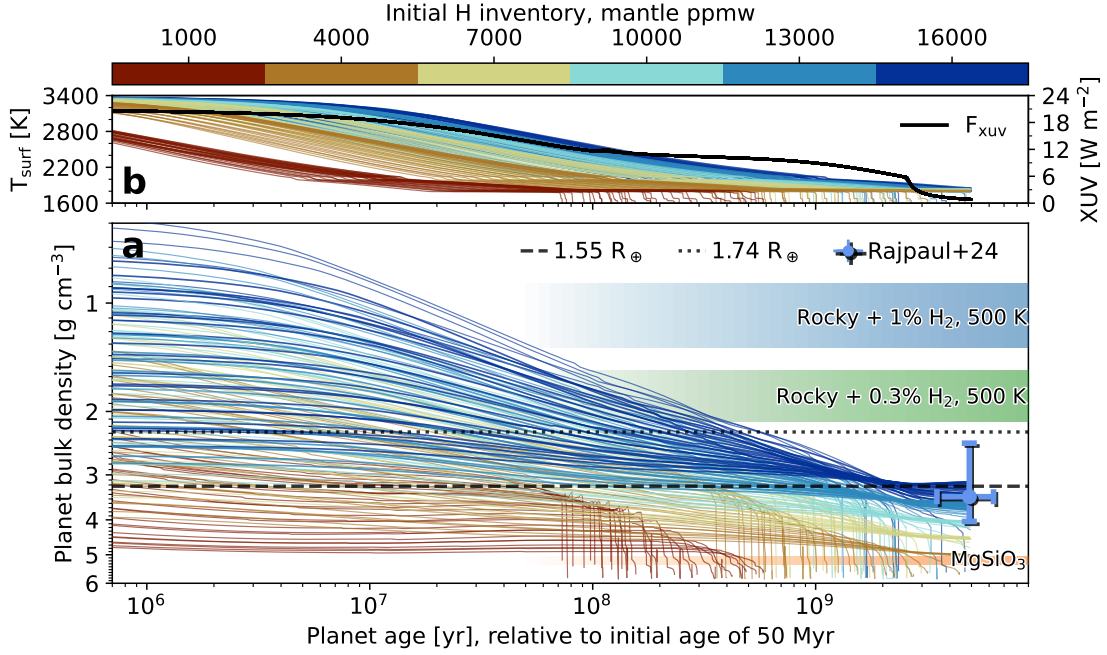


Figure 1: Modelled planetary bulk-density over time. The initial hydrogen inventory of each bulk-density evolution track is shown by the line colour. Blue/green shaded regions are reference densities for a planet of this mass (Zeng et al., 2019). Black dashed/dotted lines demarcate edges of the radius valley (at this planet mass) for low mass stars (Ho et al., 2024). The region $\pm 1\sigma$ compatible with the estimated bulk-density of this planet is indicated by the blue errorbar (Rajpaul et al., 2024; Demangeon et al., 2021). Top panel: evolution of surface temperature (coloured) and stellar XUV energy flux (black). For visual clarity, this figure only shows cases with $S/H=8$.

narios (see Supplementary Information): birth volatile endowment is thought to vary substantially (Zeng et al., 2019; Venturini et al., 2020) in addition to magma ocean oxygen fugacity (Lichtenberg and Miguel, 2025; Schlichting and Young, 2022) which controls the solubility and speciation of volatiles (Gaillard et al., 2022; Krissansen-Totton et al., 2024). Models terminate at the planet’s estimated age of (4.94 ± 1.44) Gyr or at mantle solidification; we do not model secondary volcanic outgassing from magmatism during solid-state mantle convection. Simulation endpoints are then compared with observational constraints on the planet’s density and atmospheric MMW, enabling the inference of the planet’s possible thermal and compositional histories.

Modelled evolutionary tracks (Fig. 1) show that the bulk-density ρ_p of L 98-59 d must have changed significantly over time. For the larger initial volatile inventories (blue lines), ρ_p is typically less than 2 g cm^{-3} during the first several Myr of evolution. The planet’s observable radius (measurable in transit; see Methods) initially exceeds the $1.7R_\oplus$ value often taken as the transition between the super-Earth and sub-Neptune regimes. Some cases stay within the canonical sub-Neptune regime for 950 Myr. Radiative energy losses lead to cooling and atmospheric contraction, causing the planet’s radius to evolve past the sub-Neptune edge of the radius valley (dotted line, Fig. 1a). After several Gyr of evolution up to the present day, scenarios born volatile rich with $H_{\text{ppmw}} \gtrsim 13000$ (CNHOS volatiles $\gtrsim 1.8\%$ of the planet’s mass) fall within estimates of this planet’s bulk-density, and thereby reproduce the observations.

The mantle solidifies under volatile-poor formation scenarios (Fig. 1, maroon lines) from 70 Myr onwards. Surface cooling and near-complete escape of degassed volatiles leads to a finally rapid increase in ρ_p towards that of a rocky composition within 650 Myr. These volatile-stripped scenarios are not com-

patible with the observed ρ_p despite starting with likely larger H endowments than the inner Solar System planets (Krijt et al., 2023). These cases reflect prior suggestions that airless planets may be the stripped interiors of evolved sub-Neptunes (Lopez, 2017; Owen and Wu, 2017).

Which scenarios are compatible with the observations? Fig. 2 plots modelled ρ_p at ages corresponding to the present-day. Values of ρ_p are projected over the grid axes (panels a, b, c, d) and other variables. All cases compatible with the observed ρ_p (orange points) exhibit MMWs from 7 to 24 g mol^{-1} (panel e); a spread wider than the $\pm 1\sigma$ range of $9.18^{+2.51}_{-2.41} \text{ g mol}^{-1}$ (purple line) derived with JWST. Simultaneously applying the density and MMW constraints yields the smaller cluster of blue points.

Formation with $H_{\text{ppmw}} < 10000$ can be ruled-out on the basis of ρ_p alone (grey points, Fig. 2a). We conservatively compare our model against the maximum estimate of ρ_p in the literature, and are thus not sensitive to its quoted uncertainty. Potentially larger escape efficiencies would necessitate even more volatile-rich birth scenarios to satisfy the present-day ρ_p (see Supplementary Information).

Fig. 2b shows that magma ocean oxygen fugacity fO_2 (expressed in log-units relative to the iron-wüstite buffer) must be between $IW - 4$ and $IW - 1$ in order to reproduce the observed ρ_p and MMW. More oxidising conditions favour gas speciation towards O-bearing species, increasing the atmospheric MMW. A modest MMW ($\sim 9 \text{ g mol}^{-1}$) lowers the atmosphere’s propensity for escape through a decreased radius. Larger MMW atmospheres are either over-dense or inconsistent with the JWST transit depths (or both). The full range of initial S/H mass ratio considered is compatible with the observed ρ_p . Planet mass itself has little impact on ρ_p .

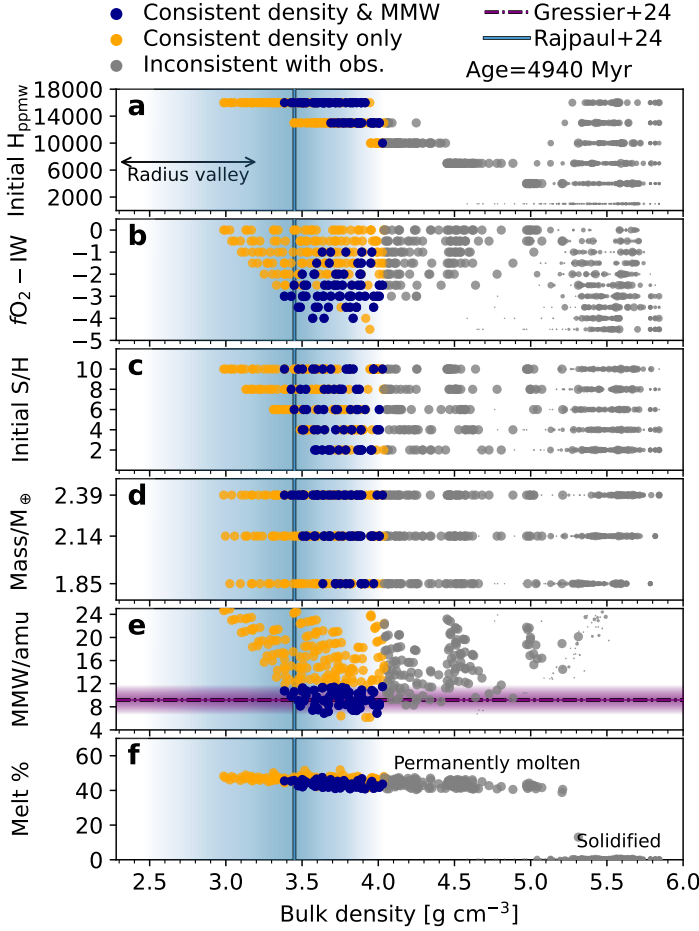


Figure 2: Projection of planetary bulk-density ρ_p against several variables. Point sizes represent the age of the planet at simulation end-points; largest sizes correspond to the present day. Vertical blue line and shaded region ($\pm 1\sigma$) highlights the observationally estimated ρ_p . Horizontal purple line show estimates on MMW (with $\pm 1\sigma$ shaded) and H_2S from free chemistry retrievals. Blue points are consistent with the observed density and MMW, orange points are only consistent with the observed density.

All outcomes compatible with the observed ρ_p fall into a tidally-heated regime with a strong atmospheric greenhouse effect. This result suggests that L 98-59 d presently retains a permanent magma ocean ($\sim 45\%$ melt fraction, Fig. 2f). A solidified mantle is ruled-out by ρ_p alone, without invoking the MMW constraint, making this result insensitive to uncertainties on the JWST observations and retrievals. The narrow range of mantle melt fractions corresponding to the observed ρ_p is a physical outcome: mantle viscosity increases strongly for melt fractions $\lesssim 45\%$ (Costa et al., 2009), making energy transport through the planet’s interior inefficient, and thereby allowing atmospheric blanketing and tides to keep a permanent magma ocean (Nicholls et al., 2025a). Insufficiently thick atmospheres lead to mantle solidification.

Many scenarios *initially* have large radii on the sub-Neptune side of the radius valley (Fig. 1). To understand how volatile loss and thermal contraction drive the marked increase in ρ_p over time, crossing through the radius valley, we study a case compatible with the observations in detail. The case study in Fig. 3 shows L 98-59 d losing 26% of its total volatile inventory whilst retaining a large surface pressure of 30 kbar (pink bars) at the present-

day. Some volatiles are outgassed; due to incomplete mantle solidification, the majority remain dissolved in the magma ocean. The atmosphere S/H mass ratio increases by a factor of 8.2 during its evolution because S, which is more soluble than H, is outgassed as the magma ocean crystallises from the bottom up (Namur et al., 2016; Gaillard et al., 2022).

Thermal contraction explains large changes in ρ_p . The surface cools from 3360 to 1830 K over the first 1.2 Gyr, corresponding to planet deflating from $> 2.2R_\oplus$ to $\sim 1.74R_\oplus$ during that period. The evolving temperature-radius profile is visualised in Fig. 3b. Early contraction is an established theoretical behaviour of H_2 -dominated envelopes and is important in regulating the rate of photoevaporative volatile loss (Kubyskhina et al., 2020; Lopez and Fortney, 2014). The atmosphere has a deep radiative layer, up to ~ 5000 km thick, above which it undergoes dry convection and is then weakly inverted. High temperatures make radiative diffusion efficient at transporting energy. Radiative layers in the deep atmosphere decreases the lapse rate, compared to an adiabat, acting to inflate the atmospheric radius *for a given surface temperature* during the planet’s evolution (see Supplementary Information). Many models in the literature assume (pseudo-)adiabatic profiles, neglecting this important impact of energy transport on atmospheric structure.

Tidal forces deposit heat energy into the planet’s mantle (Nicholls et al., 2025a) meanwhile escape continues to reduce the observable radius down to its observed value. The magma ocean buffers the atmosphere’s composition based on volatile solubility into the melt, alongside equilibrium chemistry. Dissolution of sulfur (Fig. 3a) enables the planet’s S inventory to be retained across Gyr timescales. It has been previously suggested for H_2O (Dorn and Lichtenberg, 2021) and N-compounds (Shorttle et al., 2024) that retention of volatiles in deep magma oceans buffers atmospheric escape over deep time. Analogues of mercurian lavas have established the capacity for reducing melts to take up large sulfur inventories (Namur et al., 2016).

Formation of SO_2 from H_2S , in the presence of OH radicals from photolysis H_2O , can explain the detections of SO_2 . This mechanism produces SO_2 within the hot-Jupiter WASP-39b Tsai et al. (2023); Powell et al. (2024). We infer the formation of SO_2 by making a comparison between VULCAN photochemical kinetics models and the free-chemistry retrievals. Fig. 4 plots atmospheric mixing ratios for this case study under three chemical paradigms: VULCAN SNCHO photochemical kinetics (solid lines), kinetics without photochemistry (dashed lines), and the equilibrium volatile outgassing applied during our evolutionary calculations (triangle markers at surface). The mixing ratio of SO_2 (solid blue line) increases with altitude for $p < 6$ bar, while the equivalent case without photochemistry (dashed blue line) quenches at negligible abundance. Photochemical production of SO_2 is necessary to raise its abundance to that consistent with the JWST observations (scatter points). Lime-coloured profiles show that H_2S abundance is consistent with the observational constraints under all three chemical paradigms; H_2S is thermochemically favoured to carry sulfur in the H_2 -rich background.

Detections of SO_2 cannot be explained by volcanism at the surface (Nicholls et al., 2025a), which would require SO_2 to be transported into the observable upper atmosphere without being thermochemically reduced. Transport of SO_2 (64 g mol^{-1}) would have to take place in the absence of deep convection (Fig. 3b) and therefore only by diffusion through the H_2 background. This physically unlikely scenario instead points to the formation of SO_2 in-situ, requiring only the presence of otherwise poorly-constrained H_2O . This finding represents the first indication

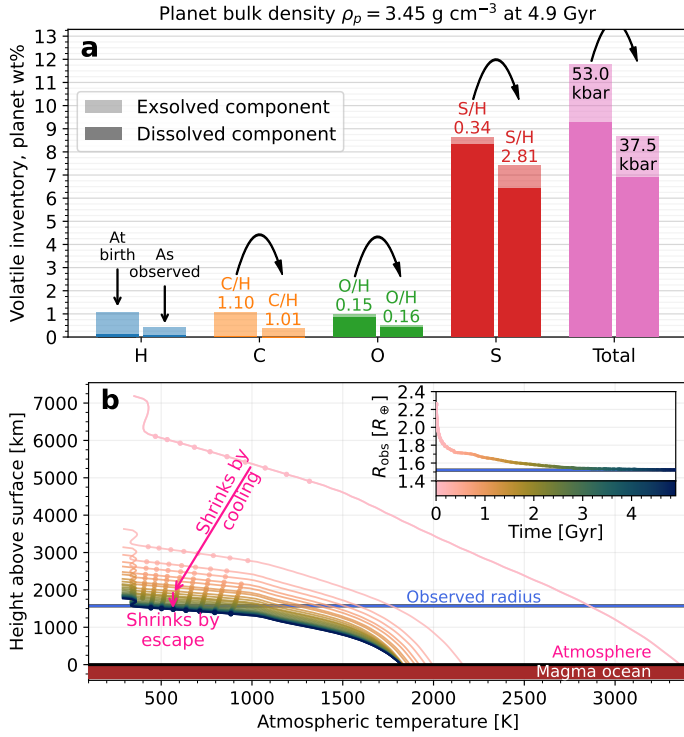


Figure 3: Volatile loss and envelope contraction over time. The changing bar heights in the top panel (a) reveal the loss of volatile elemental inventory between ‘birth’ (following boil-off) and ‘observation’ (present day) measured in percentage units relative to the planet’s total mass. Bar opacity shows the change in partitioning between the interior and atmosphere; labelled are the atmospheric mass ratios relative to H, with an enhancement of atmospheric S/H over time. The bottom panel (b) visualises the evolving atmospheric temperature-height profile, showing initially rapid contraction and cooling of the atmosphere, and the later-stage contraction from escape. Convection indicated with dots.

of active sulfur photochemistry occurring on a super-Earth exoplanet, and highlights the chemical interactions which link deep planetary interiors and their observable atmospheres.

Our modelled interior-atmosphere evolution pathways connect the observed bulk-density of L 98-59 d to a narrow range of conditions at birth. Conditions compatible with observations are those in which the planet initially had $\gtrsim 100$ times the estimated hydrogen content of the early Earth (Krijt et al., 2023). The majority of this planet’s H and C are stored in its atmosphere, whilst its S remains primarily dissolved within its chemically-reducing magma ocean. Fractionation of planetary H-C-S inventories between their interiors and atmospheres presents an opportunity for testing whether small, low-density exoplanets have underlying magma oceans through measurements of their atmospheric composition (Shorttle et al., 2024; Dorn and Lichtenberg, 2021; Kite et al., 2016).

L 98-59 d’s radius is too small for it to be classified as a prototypical sub-Neptune, although had it been observed at an age of $\lesssim 1$ Gyr we may have confidently labelled it as one (Fig. 1a). The slow transition from the sub-Neptune to super-Earth regime occurs only after several Gyr of evolution, suggesting that even relatively old sub-Neptunes with ages $\gtrsim 1$ Gyr may exist in a transient state towards becoming what would be classified as super-Earths. This Gyr-scale contraction has been suggested to explain

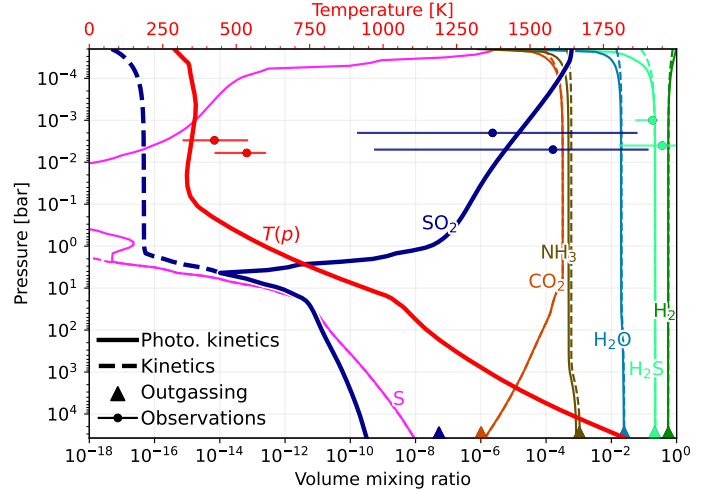


Figure 4: Atmospheric composition and temperature profiles. Solid lines plot the volume mixing ratios for a selection of gases calculated with VULCAN’s SNCHO photochemical kinetic network. Dashed lines plot mixing ratios calculated without photoreactions. Scatter points show retrieved abundances and temperatures near the photosphere (Gressier et al., 2024; Banerjee et al., 2024). We assume a modest K_{zz} of $10^5 \text{ cm}^2 \text{ s}^{-1}$ and use the radiative-convective temperature solution obtained by AGNI (thick red line).

radius-age trends in the Kepler survey (David et al., 2021) as an alternative to the ‘loss and revival’ mechanism (Kite and Barnett, 2020). Super Earths born volatile-metal rich may represent the best prospects for detections of retained atmospheres in the Rocky Worlds DDT (Ji et al., 2025); our models provide a framework for interpreting future observations of L 98-59 d alongside similar survey targets. For example, GJ 806 b also has a bulk-density consistent with a volatile atmosphere (Palle, E. et al., 2023) and represents an additional opportunity for probing the thermal and compositional evolution of super-Earth exoplanets.

L 98-59 d currently has a radius commensurate with a canonical super-Earth planet and contains a large amount of volatiles. A modestly large atmospheric MMW means that it is not an evolved gas-dwarf. Our models also show that a water-world composition is not required to explain its current bulk-density; forming significant quantities of H_2O also requires oxidising conditions incompatible with the observed transmission spectrum. Thermal contraction, magma ocean dissolution, tidal heating, and photoevaporation have shaped the radius and composition of L 98-59 d over its lifetime, and may continue doing so for billions of years.

2 METHODS

2.1 Modelling framework

We use `PROTEUS` to simulate the time evolution of L 98-59 up to the present day (Lichtenberg et al., 2021; Nicholls et al., 2024b, 2025a). `PROTEUS` is a self-consistently coupled modular simulation framework which nominally uses the `SPIDER` interior evolution model (Bower et al., 2018, 2022) and the `AGNI` radiative-convective atmosphere model (Nicholls et al., 2024a, 2025b), with atmospheric composition determined by equilibrium thermochemistry and the solubility of volatiles into the magma ocean (Gaillard et al., 2022; Sossi et al., 2023).

The pure-MgSiO₃ molten mantle is initialised on an adiabat, and evolved over time by `SPIDER` according to the energy fluxes at each radial level. The initial specific entropy is set to 3000 J K⁻¹ kg⁻¹; the planet’s subsequent evolution is insensitive to this exact value. Mixing-length theory convection, solid-liquid phase separation, grain gravitational settling, radiogenic heating, core cooling, and tidal heating are included. Tidal heating rates are calculated using `LOVEPY` with a viscoelastic Maxwell rheology (Hay et al., 2020). As in several previous studies (e.g. Bower et al., 2022; Lichtenberg et al., 2021; Hamano et al., 2015; Schaefer et al., 2016; Nicholls et al., 2024b) we do not spatially resolve energy transport *within* the metallic core, and instead fix its bulk density and heat capacity to representative Earth-like (Dziewonski and Anderson, 1981) values of 10.738 g cm⁻³ and 880 J K⁻¹ kg⁻¹ following (Bower et al., 2018). A pure Fe core of the same relative radius would be denser in L 98-59 d compared to Earth, due to compression by mantle overburden pressure. This effect of compression would be offset by incorporation of lighter elements (SNCHO, etc.) into the core, decreasing its density compared to pure Fe (Luo et al., 2024; Hirose et al., 2021). We fix the core bulk density as a constant; sensitivity tests assess the effect of interior structure (via core radius fraction as a proxy) on our results (see Supplementary Information). Heat energy is transported across the core-mantle-boundary following (Bower et al., 2019). `SPIDER` uses the (Wolf and Bower, 2018) equation of state for MgSiO₃ melt; mantle density is independent of dissolved volatile content, which can be neglected in the modelled regime (Dorn and Lichtenberg, 2021). The core radius is nominally fixed at 55% of the interior radius (see sensitivity test in Fig. 7), consistent with the relative size of Earth’s core (Lodders and Fegley, 1998). The radius R_{int} of the planet’s interior (silicate mantle plus metallic core) is calculated using `SPIDER` by solving for its hydrostatic structure for a given interior mass $M_{\text{int}} = M_p - M_{\text{atm}}$. For this planet’s $M_p = 2.14M_{\oplus}$, we typically obtain $M_{\text{core}} = 3.9 \times 10^{24}$ kg = 0.66 M_{\oplus} and $M_{\text{mant}} = 8.85 \times 10^{24}$ kg = 1.48 M_{\oplus} . The interior radius R_{int} is held constant throughout each simulation; thermal contraction and mantle solidification does not significantly affect the volume of silicate mantles (Boley et al., 2023; Unterborn and Panero, 2019; Lichtenberg and Miguel, 2025).

Energy transport through an optically-thick atmosphere regulates the planet’s energy balance. At each time-step, our radiative-convective atmosphere model `AGNI` calculates the net atmospheric energy flux for the outgassed atmospheric composition, instellation flux, and top-of-mantle temperature. The energy fluxes at each atmosphere level are calculated using `SOCRATES` (Edwards and Slingo, 1996; Amundsen et al., 2014) correlated- k two-stream ($\theta_{\text{zen}} = 54.74^\circ$) radiative transfer with 48 nominal spectral bands, including Rayleigh scattering and non-grey surface emissivity. Mixing-length convection (Joyce and Tayar, 2023) is applied, accounting for Schwarzschild-stable layers. An energy-conserving atmospheric solution is obtained using the Newton-

Raphson method with line-search. The incorporation of a real gas EOS formulation into `AGNI` is discussed within the Supplementary Information.

Stellar evolution is modelled using `MORS` (Johnstone et al., 2021). We take L 98-59 to have a mass 0.273 M_{\odot} and rotation rate 80.9 day at the present day (Engle and Guinan, 2023). `MORS` uses a shell rotation model with empirically-derived scalings to estimate the bolometric and XUV emission from the star over its lifetime. The estimated X-ray luminosity at the present day is consistent with XMM Newton observations (Behr et al., 2023; Nicholls et al., 2025a). We use the L 98-59 spectrum from the `MUSCLES` Extension (Behr et al., 2023). Stellar quantities are updated throughout the simulations; changes in stellar flux are appropriately reflected in the atmospheric temperature, albedo, and escape rate.

All simulations are initialised at a planet age of 50 Myr relative to the formation of the system, under the assumption that boil-off has completed (Tang et al., 2024, see Supplementary Information) and further delivery processes are negligible compared to the physics and timescales simulated (Lichtenberg et al., 2023). Simulations terminate when the simulated age reaches the 4.94 Gyr estimated age of L 98-59 (Engle and Guinan, 2023) or when the mantle solidifies (melt-fraction $\Phi < 0.5\%$). We do not simulate mantle evolution post-solidification; solid-phase volatile partitioning (Hier-Majumder and Hirschmann, 2017; Sim et al., 2024) and volcanic outgassing (Liggins et al., 2022) are not included, as the associated mass fluxes are several orders of magnitude below those of magma ocean degassing (Lichtenberg and Miguel, 2025; Gaillard et al., 2021). Cases consistent with the observations are those with a planet bulk-density ρ_p comparable ($\pm 1\sigma$) with its most up-to-date estimate of 3.45 g cm⁻³ (Rajpaul et al., 2024). The bulk-density $\rho_p = 3M_p/4\pi R_p^3$ depends on the total planet mass M_p and the observable radius R_p that would be photometrically probed in transit. M_p includes the mantle, metallic core, dissolved volatiles, and atmosphere. The observable radius R_p is determined by the radius corresponding to the 20 mbar pressure level (Lehmer and Catling, 2017), to which our results are not sensitive.

Atmospheric escape is introduced into the `PROTEUS` framework through a new module, detailed in the section below.

2.2 Energy-limited escape

Our escape module implements the classic energy-limited formulation of photoevaporative gas loss,

$$\Phi_{\text{hyd}}(t) = \frac{\eta\pi[R_{\text{XUV}}(t)]^3 F_{\text{XUV}}(t)}{GM_p}, \quad (1)$$

which assumes that stellar XUV flux F_{XUV} absorbed by an optically thick disk of radius R_{XUV} lifts mass at a rate Φ_{hyd} out of the gravitational potential-well with efficiency η , at each point in time t . The time-dependent $F_{\text{XUV}}(t)$ is calculated with `MORS` (Johnstone et al., 2021). $R_{\text{XUV}}(t)$ is determined from the atmospheric temperature structures calculated by `AGNI` (see Supplementary Information), taking $P_{\text{XUV}} = 5$ Pa (Lehmer and Catling, 2017).

An atmosphere composed of hydrogen and high-MMW elements will experience compositional fractionation at varying degrees depending on the XUV irradiation, collisional coupling between species, and gravity. In the limit of rapid hydrodynamic escape, and where the high-MMW elements compose a significant fraction of the atmosphere by mass, hydrodynamic simulations from

(Johnstone, 2020) have shown that the thermosphere is expected to escape in bulk without fractionating. Here, we explore high-MMW atmospheres exposed to XUV fluxes greater than a hundred times present Earth levels, so we adopt this approximation of no thermospheric fractionation. Including fractionation would not change our major conclusions, as it would only enhance the S/H ratio, all else equal.

We adopt a 10% escape efficiency (Lehmer and Catling, 2017; Owen, 2019), which agrees with simulations from (Yoshida et al., 2024) that account for molecular line cooling (see discussion in Supplementary Information). The elemental composition of the escaping gas is set equal to that of the outgassed atmosphere, which would be photodissociated and partially photoionised on outflow. To calculate the loss rate of each element from the planet’s *total* volatile inventory, we proportion the bulk escape rate by the *atmospheric* mass mixing ratios of each element. While the escape process itself is treated as non-fractionating, it acts upon an *atmospheric* elemental composition different to the *bulk* planetary composition. Volatile loss can thereby fractionate the planet’s elemental inventories as a result of volatile interior-atmosphere partitioning.

3 SUPPLEMENTARY INFORMATION

3.1 Observed planetary parameters

Table 1 outlines the most recent estimates for the orbital and bulk parameters of L 98-59 d, derived from the NASA Exoplanet Archive. It has a zero-albedo equilibrium temperature of 416 K (Demangeon et al., 2021). Note that the planet radius R_p represents the observable radius of the planet at the level probed photometrically during transit (primary eclipse); R_p is not equal to the radius of the surface.

The orbital eccentricities estimated for L 98-59 b/c/d have previously merited an investigation into the stability of this system. Taking median estimates for e and a on each planet yields an unstable orbital configuration; stability is readily achieved by adjusting eccentricity of only planet c from 0.147 to 0.103, while leaving the other planets unperturbed (Demangeon et al., 2021).

3.2 Modelling atmospheric structure

Atmospheric thermal $T(P)$ and structural $r(P)$ evolution is an important factor in setting the atmospheric escape rates of young sub-Neptune planets following formation (Lopez and Fortney, 2014; Kubyskhina et al., 2020). The small molar mass of H_2 and high temperatures mean that sub-Neptune atmospheres are initially inflated, allowing for efficient ‘boil-off’ (Tang et al., 2024). This propensity for early volatile loss could extend to lower mass planets (Lehmer and Catling, 2017), especially those orbiting pre-main sequence stars with large XUV luminosities during their saturated phase (Johnstone et al., 2021).

An accurate representation of atmospheric structure is important for comparing models to observations, and for accurately modelling atmospheric escape rates. Several previous studies on early atmospheric structural evolution and escape have assumed convective temperature profiles (e.g. Rogers, 2025; Cherubim et al., 2025; Krissansen-Totton et al., 2024; Lehmer and Catling, 2017; Wordsworth and Pierrehumbert, 2013; Rogers, 2015). However, it has been shown that convectively-stable deep radiative layers can form (Innes et al., 2023; Selsis et al., 2023; Nicholls et al., 2024a). Compared to an adiabatic profile, the shallow lapse rates (dT/dp) of dry radiative layers yield cooler surfaces and hotter upper-atmospheres at radiative equilibrium. For a *given* surface

temperature T_s , radiative layers yield larger atmospheric temperatures.

Here, the atmosphere is defined on a pressure grid of 40 layers between the top P_t and the surface P_s . The surface pressure evolves over time, calculated at each step by our volatile outgassing scheme (Nicholls et al., 2024b; Sossi et al., 2023; Shorttle et al., 2024). P_t is fixed at 1 Pa. Assuming that the atmosphere is hydrostatically self-supported, we relate the pressure and radius

$$dP = -\rho(P, T)g(r)dr, \quad (2)$$

where $\rho(P, T)$ is the mass-density of the gas at pressure P and temperature T , $g(r)$ is the gravitational acceleration, and r is the radial distance from the planet centre. Equation 2 is integrated from P_s to P_t . The radius $r = R_{\text{int}}$ and gravity at the surface are calculated by SPIDER as described above. The first improvement made for this work is to express the gravity $g(r)$ at each layer as

$$g(r) = \frac{G}{r^2}M(r) \quad (3)$$

where $M(r)$ is the *total* mass enclosed within r , accounting for the gravitational attraction of the upper atmosphere layers to the atmosphere layer below (as well as to the planet interior). Self-attraction is important for these atmospheres which comprise percentage-fractions of the total mass. AGNI now also implements an RK4 scheme to integrate Equation 2, using 30 sublevels within each of the atmosphere layers.

The second improvement here is the implementation of a real-gas EOS, used to evaluate $\rho(P, T)$ in Equation 2 and adiabatic lapse rate ∇_{ad} . Whenever the atmospheric composition or temperature is updated, the densities ρ_j of each volatile component j are re-evaluated separately using their appropriate EOS, and then combined using Amagat’s additive volume law to obtain the total mass-density ρ at each layer:

$$\frac{1}{\rho(P, T)} = \sum_j \frac{1}{y_j \rho_j(P, T)}, \quad (4)$$

where y_j are mass mixing ratios. This construction permits non-ideal behaviour for each gas component, but assumes that species mix without interacting. Ideal mixing has long been applied in stellar physics (Dorman et al., 1991; Saumon et al., 1995; Baraffe et al., 2015) and for H_2 -dominated planetary atmospheres (Kubyskhina et al., 2020; Paxton et al., 2011). Lab experiments and DFT simulations have shown that ideal mixing is robust and provides the flexibility necessary for modelling mixtures at extreme conditions (Magyar et al., 2014, 2015; Bradley et al., 2018). The EOS for water is interpolated from (Haldemann et al., 2020) and the EOS for hydrogen is interpolated from (Chabrier et al., 2019). The Van der Waals EOS is applied for CO_2 , CH_4 , CO , N_2 , NH_3 , SO_2 , H_2S , and O_2 . Any other gases are treated as ideal.

To validate our updated atmospheric structure calculation, here we apply AGNI to a range of binary H_2 - H_2O mixtures. The atmosphere of L 98-59 d is thought to be mainly composed of H_2 , with volatiles of higher MMW mixed-in (Gressier et al., 2024; Banerjee et al., 2024; Demangeon et al., 2021). We use H_2O as a proxy for heavy species here because of its particular potential for non-ideal behaviour. Fig. 5 plots modelled atmospheric structures for a range of H_2 - H_2O mixtures (line colour), EOS formulations (rows), and temperature profile assumptions (line style). Solid lines are radiative-convective models where an energy-conserving solution is obtained for a given instellation, and given surface temperature T_s (3000 K) and pressure P_s (1000 bar). Dashed lines are defined by the dry adiabat until they

Parameter	Demangeon et al. (2021)	Rajpaul et al. (2024)	Luque and Palle (2022)	Cloutier et al. (2019)
a [0.01 AU]	$4.86^{+0.18}_{-0.19}$	–	–	5.06 ± 0.02
Eccentricity	$0.074^{+0.057}_{-0.046}$	$0.098^{+0.027}_{-0.096}$	–	< 0.09
R_p/R_\oplus	$1.521^{+0.119}_{-0.098}$	$1.521^{+0.119}_{-0.098}$	1.58 ± 0.08	1.57 ± 0.14
M_p/M_\oplus	1.94 ± 0.28	$2.14^{+0.25}_{-0.29}$	$2.31^{+0.46}_{-0.45}$	$2.31^{+0.46}_{-0.45}$
ρ_p [g cm ⁻³]	$2.95^{+0.79}_{-0.51}$	$3.45^{+0.25}_{-0.29}$	$3.17^{+0.85}_{-0.73}$	$3.3^{+1.3}_{-0.9}$

Table 1: Literature estimates for the pertinent parameters of the planet L 98-59 d. Tabulating semi-major axis a , orbital eccentricity e , planet radius R_p , planet mass M_p , and bulk-density ρ_p . Mass and density (Rajpaul et al., 2024) were obtained through a combined re-analysis of HARPS (Cloutier et al., 2019) and ESPRESSO datasets (Demangeon et al., 2021). The extreme $\pm 1\sigma$ range on the bulk-density across these four works is 2.4 to 4.6 g cm⁻³.

intersect the H₂O saturation curve: an assumption typically applied in the literature. Note that these profiles are calculated for a fixed T_s , which represents the early phase of atmospheric evolution above a hot magma ocean, and not at radiative equilibrium (which occurs after Gyr-scale time evolution).

Panels (a) and (b) of the figure show that the radiative-convective profiles (solid lines) are not always on the corresponding adiabat (dashed lines). Stellar radiation heats the upper layers, while thermal radiative diffusion efficiently carries the energy flux in deeper regions. The corresponding radius profiles are plotted in panels (c) and (d), with H₂-rich low MMW models yielding extended envelopes.

Panel (c) shows that assuming a fully-convective structure (dashed lines) acts to deflate the atmosphere, while energy conserving solutions (solid lines) are more inflated for the given T_s . In H₂O-poorest scenarios (red lines), radiative heating inflates the atmosphere from ~ 4000 to ~ 7300 km (+83%), whereas the H₂O-richest case is inflated by +33%. Gas escape rates are closely linked to atmospheric radius through equation 1, so our radiative-convective model captures the realistic enhancement to photoevaporation here.

Panel (b) shows real-gas temperature profiles corresponding to the ideal-gas equivalents in panel (a). Negligible differences between panels show that the EOS formulation only marginally impacts the temperature structure. The choice of EOS matters only when a simplified adiabatic temperature structure is assumed (compare dashed lines between panels c and d) because adiabatic profiles enter into a non-ideal regime. Radiative-convective solutions remain sufficiently hot for the gas to behave ideally. Correspondence between our real and ideal EOS formulations, where expected, demonstrates that our real-gas EOS formulation is behaving correctly.

We employ realistic modelling of atmospheric temperature and radius structure, which ensures energy conservation through each model layer. Although Fig. 5 shows that the ideal gas EOS can be safely applied, we also employ our real gas EOS formulation for completeness.

3.3 Inclusion of additional volatile species

Considering the observational indications of H₂S in the atmosphere of L 98-59 d, we update our outgassing scheme (Nicholls et al., 2024b) to include H₂S. The partial pressure formed by the exothermic net reaction $S_2 + 2H_2 = 2H_2S$ is determined by K_{eq} at thermochemical equilibrium. Given the relation $K_{eq} = \exp(-\Delta G/RT)$, where ΔG is the reactional change in Gibbs free energy, this equation lets the model account for the speciation of

sulfur and hydrogen into H₂S within the atmosphere overlying the magma ocean. The NIST-JANAF database tabulates ΔG for S₂ and H₂S as a function of temperature. The equilibrium constant of this reaction is fitted as $K_{eq}(T) = \exp(a/T - b)$ where $a = 6731.02$ K and $b = 3.62273$, valid from 200 to 4000 K. This reaction is exothermic, so H₂S is expected to form favourably at surface temperatures near or after mantle solidification. Consistency between lime-coloured H₂S profiles in Fig. 4 shows that this net reaction independently reproduces the same behaviour as VULCAN’s full chemical network.

Hydrogen-rich atmospheres could also allow for the formation of NH₃. Non-detection of NH₃ in the sub-Neptune K2-18 b is central to the ongoing discussion as to its surface conditions, as NH₃ could be readily dissolved in either a magma ocean or water ocean (Shorttle et al., 2024; Madhusudhan et al., 2023). We also include the formation of ammonia through the reaction $3H_2 + N_2 = 2NH_3$. This reaction is well fitted with $a = 2664.02$ K and $b = 5.99238$.

3.4 Bracketing our parameter space

The planet’s initial inventory of volatiles is defined in our model by:

- H_{ppmw} , the total mass of hydrogen relative to the mass of the mantle.
- S/H, the amount of sulfur in the planet relative to H by mass.
- N/H, the amount of nitrogen in the planet relative to H by mass.
- C/H, the amount of carbon in the planet relative to H by mass.

The first two variables are incorporated into our main grid of simulations. Our grid also considers a range of oxygen fugacities fO_2 , which are quantified in log₁₀ units relative to the temperature-dependent iron-wüstite buffer. To maintain a computationally feasible parameter space, the C/H and N/H are fixed based on Earth’s primitive mantle (Wang et al., 2018). Defining the initial S/N/C relative to H means that H_{ppmw} acts as a measure of the initial total volatile endowment. All other quantities (e.g. mantle melt-fraction, surface temperature) are determined during the evolution by other physical processes.

We can expect that this planet contained relatively more H than Earth’s primitive mantle did after boil-off, given multiple observational indications of a present-day H₂-dominated atmosphere. A wide range of initial H inventories are covered by our main

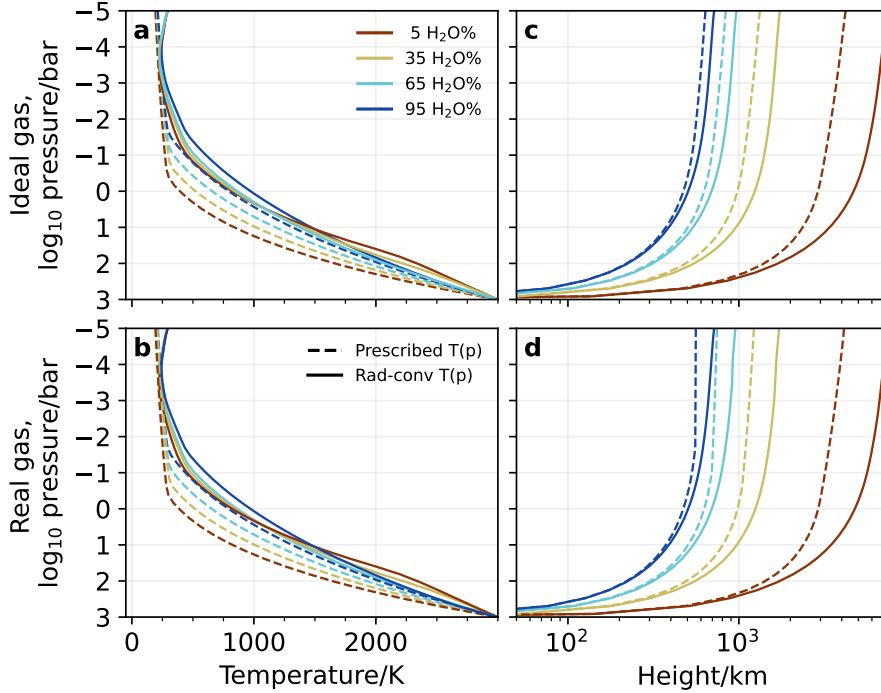


Figure 5: Atmospheric temperature (left) and radius (right) structures calculated by AGNI for a range of H₂-H₂O mixtures (line colours). The top row uses the ideal gas EOS, while the bottom row uses the real gas EOS formulation described in the text. Line style indicates whether a prescribed or energy-conserving temperature solution was obtained.

grid: from 1000 ppmw (approximately ten times that estimated for Earth’s primitive mantle; (Wang et al., 2018)) up to 16000 ppmw (i.e. 1.6 wt% relative to the mantle mass). The upper limit is a numerically-tractable value informed by the literature (Tang et al., 2024; Lopez and Fortney, 2014). Recent modelling of the core-powered mass loss of primary envelopes has suggested that no more than 1.79 wt% of hydrogen (relative to the total mass) may be retained following early boil-off, for a planet with approximately this mass and instellation (Tang et al., 2024). Our modelled mantles typically correspond to 68% of the planet’s total mass; this estimated upper limit of 1.79 wt% total hydrogen then corresponds to $H_{\text{ppmw}} \sim 26000$ relative to the mass of the mantle.

Although Earth’s upper mantle oxygen fugacity has remained nearly constant for billions of years (Trail et al., 2011), in general oxygen fugacity may evolve over time – and in particular during the magma ocean stage – due to several simultaneous processes that modulate the redox state of iron (McCammom, 1997; Wade and Wood, 2005; Itcovitz et al., 2022; Kite and Schaefer, 2021; Lichtenberg, 2021; Krissansen-Totton et al., 2024; Schaefer et al., 2024). To represent the potential diversity implied by these partly competing mechanisms, we fix oxygen fugacity fO_2 at the magma ocean surface throughout each simulation and bracket a wide range fO_2 broadly by comparing against observations (Gressier et al., 2024). The 9.18 g mol^{-1} contour in Fig. 6, equal to the molar mass inferred from retrievals, broadly rules out $fO_2 < IW - 4$ and $fO_2 > IW$. This suggests that L 98-59 d must have an interior more reducing than Earth’s mantle at $IW + 3.5$ (Nicklas et al., 2018) but more oxidising than Mercury’s surface $\sim IW - 5.4$ (Namur et al., 2016). This stand-alone calculation does not account for changes in abundances induced by escape, which are self-consistently accounted for in our evolutionary models.

S/H is not well constrained by Fig. 6 at reducing conditions; all

S/H are compatible with the retrieved MMW and H₂S depending on magma ocean oxygen fugacity. SO₂ remains a minor constituent of the atmosphere throughout the phase space as speciation of S into H₂S is preferred (see photochemical production in Fig. 4). Abundances of nearby stars and models of protoplanetary disk chemistry together indicate that a range of formation scenarios can reasonably allow rocky planets to form with more than 2% sulfur by mass, with formation scenarios exterior to the ice line generally not exceeding 10 wt% (Jorge et al., 2022; Oosterloo et al., 2025).

In summary: applying Fig. 6 alongside reasoning from established cosmochemistry and planet formation constraints provides broad bounds on the initial volatile inventory. We construct our grid of simulations with four axes:

- oxygen fugacity, $IW - 4.5 \leq fO_2 \leq IW$
- hydrogen inventory, $1000 \leq H_{\text{ppmw}} \leq 16000$
- bulk S/H mass ratio, $2 \leq S/H \leq 10$
- total planet mass, $1.85 \leq M_p \leq 2.39$

Mass is varied across the $\pm 1\sigma$ range (Rajpaul et al., 2024). This parameter configuration results in the 900 scenarios modelled in our main Results. This parameter space results in total volatile inventories between 0.1% and 10.9% of the planet’s total mass (median of 2.7%).

3.5 Sensitivity tests to model parameters

In this section we test the sensitivity of our model to several parameters not included within our main grid. We take one of the configurations from the grid which reproduces the present-day bulk-density and atmospheric MMW as a base-case, and then vary: orbital eccentricity e , escape efficiency η , metallic core radius fraction r_c , and the number of radiative transfer spectral bands.

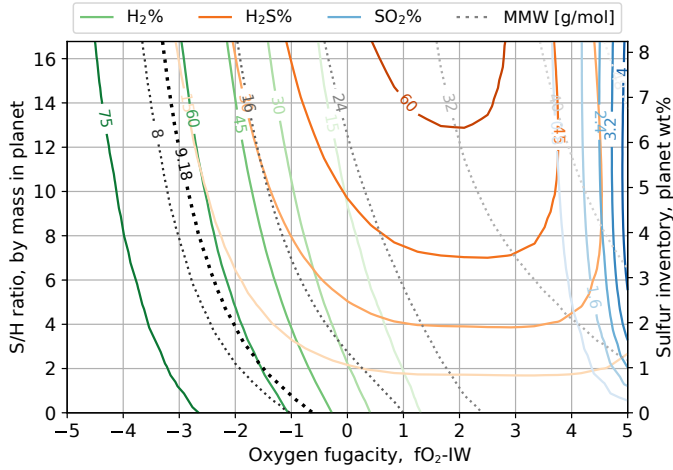


Figure 6: Modelled outgassed atmospheric compositions in equilibrium with an underlying magma ocean. Coloured contours plot the volume mixing ratios of H_2 , H_2S , and SO_2 versus bulk S/H mass ratio and oxygen fugacity. Dotted grey lines shows contours of MMW. Outgassing conditions in this plot are 1850 K with a mantle melt-fraction at 40%, representative of a planet kept semi-molten by tidal heating and an atmospheric greenhouse, $\text{H}_{\text{ppmw}} \approx 7150$, and $M = 2.14M_{\oplus}$.

Sensitivity tests plotted in Fig. 7 show that our main conclusions are robust. Panels (a) and (b) reveal a weak dependence on orbital eccentricity; only the zero-eccentricity case tends towards complete mantle solidification. Orbital evolution, not modelled here, would correspond to larger initial eccentricities and an initially increased tidal heating rate (Driscoll and Barnes, 2015). Changes to escape efficiency η have the largest impact on modelled evolution (panels b and f) across the four test suites. Increasing η to 20% leads to smaller radii and melt-fractions. Escape efficiencies of $\lesssim 20\%$ – unrealistic due to the effects of atomic line cooling (Yoshida et al., 2024) – cause the planet to lose its volatile envelope in this case (see next SI section for further analysis). Panels (c) and (g) show that our model has only minor sensitivity to core radius fractions r_c for values up to 80%. The largest r_c end-members correspond to shallow magma oceans which are readily saturated in volatiles, and thereby yield larger atmospheres for a given planetary inventory. A core compressed to $\rho_c = 15.3 \text{ g cm}^{-3}$ by overburden forces (Hirose et al., 2021) would have a radius $r_c = 49\%$ for the same mass as our nominal core configuration ($r_c = 55\%$ with $\rho_c = 10.738 \text{ g cm}^{-3}$). Minor differences between r_c of 55% and $\sim 50\%$ in Fig. 7 show that fixing ρ_c based on PREM has a negligible impact on our results. The our nominal choice of 48 correlated- k spectral bands does not bias the calculated observable radii and mantle melt fractions (panels d and h).

3.6 Escape efficiency versus volatile endowment

From the previous section, Fig. 7f points to some of our modelled outcomes potentially being sensitive to the nominal choice of 10% escape efficiency η . The total volatile loss, and thus η , is influenced by several uncertainties: the star’s rotational evolution and high-energy spectrum (Johnstone et al., 2021), and variations in escape rates from three-dimensional star-planet interactions and non-LTE cooling processes (Gronoff et al., 2020). However, we posit that sensitivity to η can be offset by variations in the planet’s initial volatile inventory. To illustrate this, we run an additional grid of simulations which span a plausible range of

these parameters: $8000 \leq \text{H}_{\text{ppmw}} \leq 30000$ and $5\% \leq \eta \leq 25\%$, also varying $f\text{O}_2 = \{\text{IW} - 2, \text{IW} - 3\}$ for completeness. A plausible upper-value on this planet’s H inventory after boil-off is $\sim 26000 \text{ ppmw}$ (see SI sections above, and (Tang et al., 2024)).

Contours of modelled bulk-density versus H_{ppmw} and η are plotted in Fig. 8 for two values of oxygen fugacity (panels). The observed density (Rajpaul et al., 2024) is indicated by the blue contour. Diagonal bands show that larger escape efficiencies necessitate larger initial volatile inventories in order to obtain a given present-day ρ_p . Taking an enhanced 15% efficiency, following the blue line in the top panel ($f\text{O}_2 = \text{IW} - 3$) shows that an initial volatile inventory $\text{H}_{\text{ppmw}} = 26000$ still results in a modelled present-day ρ_p that is consistent with the observations. Uncertainties in the observed density (dashed lines) are a more significant factor than our choice of η . Considering $\pm 1\sigma$ contours (dashed lines), both large ($\eta \approx 20\%$) and small ($\eta \approx 8\%$) escape efficiencies yield simulation outcomes (at $\text{IW} - 3$) within the observational constraints for reasonable volatile-rich scenarios. With a less reducing $\text{IW} - 2$ mantle, escape efficiencies of 20% result in present-day ρ_p falling within the observational uncertainty for a reasonable range of H_{ppmw} . These tests show that our main conclusions are robust; the H_{ppmw} modelled in Fig. 8 all represent volatile-rich formation scenarios.

DECLARATIONS

Acknowledgements

TL acknowledges support from the Netherlands eScience Center under grant number NLESC.OEC.2023.017, the Branco Weiss Foundation, the Alfred P. Sloan Foundation (AETHER project, G202114194), and NASA’s Nexus for Exoplanet System Science research coordination network (Alien Earths project, 80NSSC21K0593). CMG is supported by the UK STFC (ST/W000903/1). RTP and RDC acknowledge support from the UK STFC and the AETHER project. We thank the Center for Information Technology of the University of Groningen for their support and for providing access to the Habrok high performance computing cluster. We also thank Tad Komacek for his thoughtful suggestions, and Laurent Soucasse for his continued contributions to PROTEUS.

Author contributions

Nicholls: Conceptualization, Methodology, Software, Investigation, Writing - Original Draft, Visualization. **Lichtenberg:** Conceptualization, Methodology, Software, Writing - Review & Editing. **Chatterjee:** Conceptualization, Methodology, Writing - Original Draft. **Guimond:** Conceptualization, Writing - Review & Editing. **Postolec:** Software, Writing - Review & Editing. **Pierrehumbert:** Supervision, Writing - Review & Editing.

Code availability

All computer codes used in this work are open source software available on GitHub:

- PROTEUS, <https://github.com/FormingWorlds/PROTEUS>
- AGNI, <https://github.com/nichollsh/AGNI>
- SPIDER, <https://github.com/djbower/spider>
- LOVEPY, <https://github.com/nichollsh/lovepy>

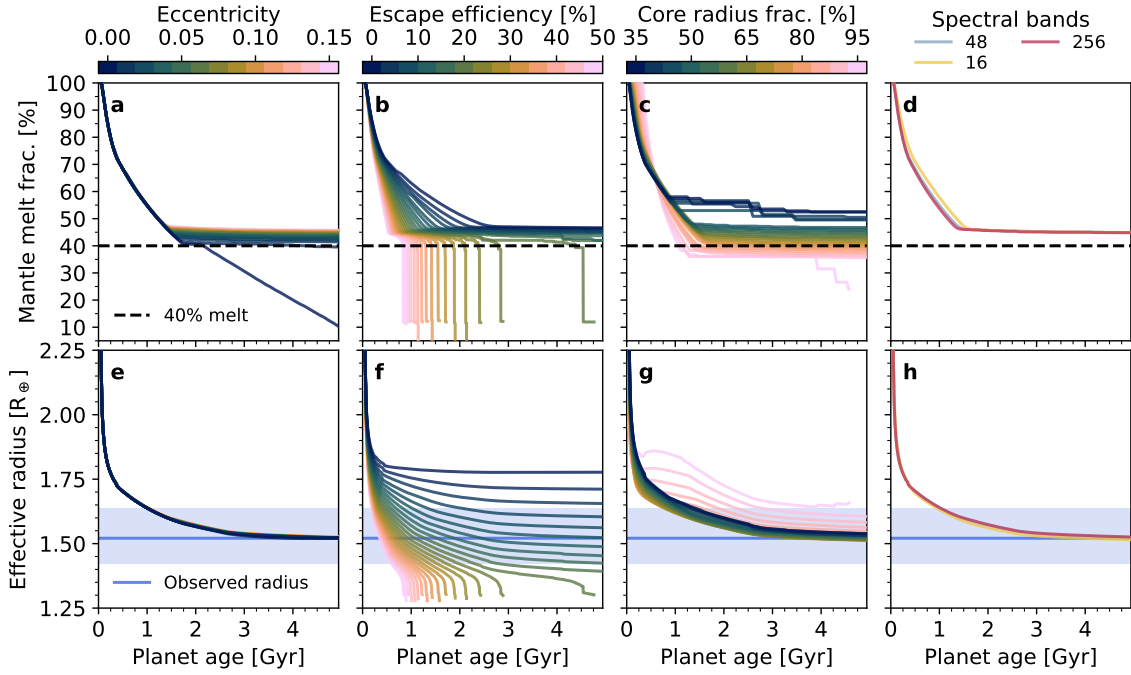


Figure 7: Sensitivity of modelled mantle melt-fraction and observable radius to model parameters. Model parameters (columns): orbital eccentricity, atmospheric escape efficiency, metallic core radius fraction, and the number of spectral bands. Sensitivity is assessed by the modelled evolutionary differences in mantle melt-fraction (top row) and the observable radius of the planet (bottom row).

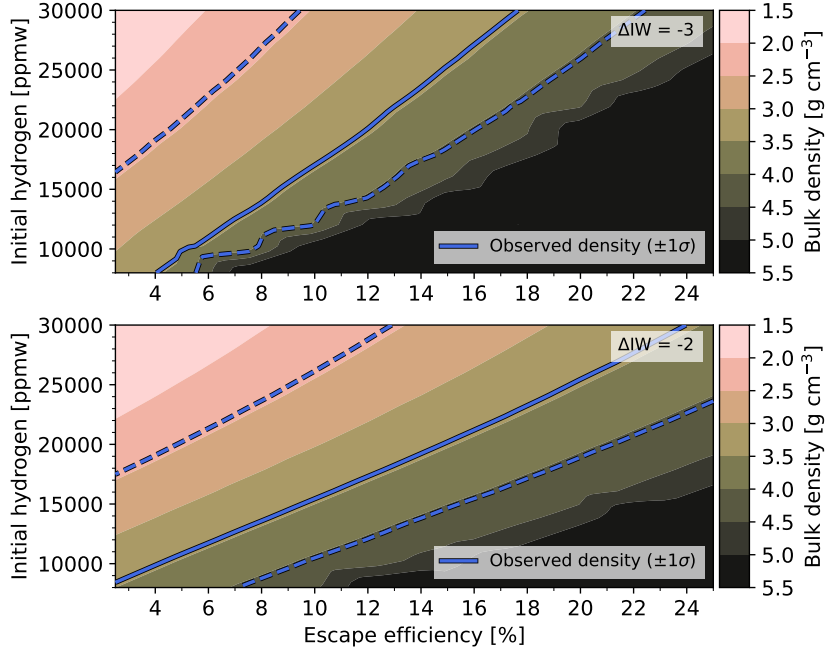


Figure 8: Contour plots of bulk density versus initial volatiles and escape efficiency shows a trade-off between these model parameters. Modelled planet bulk-density at its present age is indicated by the colour-bar. The observed density contour is shown by the blue line (solid) with its uncertainty (dashed). Calculated for two values of oxygen fugacity (top and bottom panels).

REFERENCES

- Diana Valencia, Amaya Moro-Martín, and Johanna Teske. Diversity of Exoplanets. *arXiv e-prints*, art. arXiv:2505.09754, May 2025. doi: 10.48550/arXiv.2505.09754.
- Li Zeng, Stein B. Jacobsen, Dimitar D. Sasselov, Michail I. Petaev, Andrew Vanderburg, Mercedes Lopez-Morales, Juan Perez-Mercader, Thomas R. Mattsson, Gongjie Li, Matthew Z. Heising, Aldo S. Bonomo, Mario Damasso, Travis A. Berger, Hao Cao, Amit Levi, and Robin D. Wordsworth. Growth model interpretation of planet size distribution. *Proceedings of the National Academy of Science*, 116(20):9723–9728, May 2019. doi: 10.1073/pnas.1812905116.
- James G. Rogers, Hilke E. Schlichting, and James E. Owen. Conclusive Evidence for a Population of Water Worlds around M Dwarfs Remains Elusive. *Astrophysical Journal Letters*, 947(1):L19, April 2023. doi: 10.3847/2041-8213/acc86f.
- James E. Owen and Yanqin Wu. The evaporation valley in the kepler planets. *The Astrophysical Journal*, 847(1):29, sep 2017. doi: 10.3847/1538-4357/aa890a. URL <https://dx.doi.org/10.3847/1538-4357/aa890a>.
- Rafael Luque and Enric Palle. Density, not radius, separates rocky and water-rich small planets orbiting M dwarf stars. *Science*, 377(6611):1211–1214, September 2022. ISSN 0036-8075, 1095-9203. doi: 10.1126/science.abl7164. URL <https://www.science.org/doi/10.1126/science.abl7164>.
- Remo Burn, Christoph Mordasini, Lokesh Mishra, Jonas Haldemann, Julia Venturini, Alexandre Emsenhuber, and Thomas Henning. A radius valley between migrated steam worlds and evaporated rocky cores. *Nature Astronomy*, 8:463–471, April 2024. doi: 10.1038/s41550-023-02183-7.
- Agnibha Banerjee, Joanna K. Barstow, Amélie Gressier, Néstor Espinoza, David K. Sing, Natalie H. Allen, Stephan M. Birkmann, Ryan C. Challener, Nicolas Crouzet, Carole A. Haswell, Nikole K. Lewis, Stephen R. Lewis, and Jingxuan Yang. Atmospheric retrievals suggest the presence of a secondary atmosphere and possible sulfur species on 198-59 d from jwst nirspec g395h transmission spectroscopy. *The Astrophysical Journal Letters*, 975(1):L11, oct 2024. doi: 10.3847/2041-8213/ad73d0. URL <https://dx.doi.org/10.3847/2041-8213/ad73d0>.
- Amélie Gressier, Néstor Espinoza, Natalie H. Allen, David K. Sing, Agnibha Banerjee, Joanna K. Barstow, Jeff A. Valenti, Nikole K. Lewis, Stephan M. Birkmann, Ryan C. Challener, Elena Manjavacas, Catarina Alves de Oliveira, Nicolas Crouzet, and Tracy L. Beck. Hints of a Sulfur-rich Atmosphere around the 1.6 R_⊕ Super-Earth L98-59 d from JWST NIRSpec G395H Transmission Spectroscopy. *Astrophysical Journal Letters*, 975(1):L10, November 2024. doi: 10.3847/2041-8213/ad73d1.
- Emily K Pass, David Charbonneau, and Andrew Vanderburg. The Receding Cosmic Shoreline of Mid-to-Late M Dwarfs: Measurements of Active Lifetimes Worsen Challenges for Atmosphere Retention by Rocky Exoplanets. *arXiv e-prints*, art. arXiv:2504.01182, April 2025.
- Tim Lichtenberg, Dan J. Bower, Mark Hammond, Ryan Boukrouche, Patrick Sanan, Shang-Min Tsai, and Raymond T. Pierrehumbert. Vertically Resolved Magma Ocean–Protoatmosphere Evolution: H₂, H₂O, CO₂, CH₄, CO, O₂, and N₂ as Primary Absorbers. *Journal of Geophysical Research: Planets*, 126(2), February 2021. ISSN 2169-9097, 2169-9100. doi: 10.1029/2020JE006711. URL <https://onlinelibrary.wiley.com/doi/10.1029/2020JE006711>.
- Harrison Nicholls, Raymond T Pierrehumbert, Tim Lichtenberg, Laurent Soucasse, and Stef Smeets. Convective shutdown in the atmospheres of lava worlds. *Monthly Notices of the Royal Astronomical Society*, 536(3):2957–2971, 12 2024a. ISSN 0035-8711. doi: 10.1093/mnras/stae2772. URL <https://doi.org/10.1093/mnras/stae2772>.
- Harrison Nicholls, Claire Marie Guimond, Hamish C. F. C. Hay, Richard D. Chatterjee, Tim Lichtenberg, and Raymond T. Pierrehumbert. Self-limited tidal heating and prolonged magma oceans in the 1 98-59 system, 2025a. URL <https://arxiv.org/abs/2505.03604>.
- Shang-Min Tsai, Elspeth K. H. Lee, Diana Powell, Peter Gao, Xi Zhang, Julianne Moses, Eric Hebrard, Olivia Venot, Vivien Parmentier, Sean Jordan, Renyu Hu, Munazza K. Alam, Lili Alderson, Natalie M. Batalha, Jacob L. Bean, Bjorn Benneke, Carver J. Bierson, Ryan P. Brady, Ludmila Carone, Aarynn L. Carter, Katy L. Chubb, Julie Inglis, Jeremy Leconte, Michael Line, Mercedes Lopez-Morales, Yamila Miguel, Karan Molaverdikhani, Zafar Rustamkulov, David K. Sing, Kevin B. Stevenson, Hannah R. Wakeford, Jeehyun Yang, Keshav Aggarwal, Robin Baeyens, Saugata Barat, Miguel De Val-Borro, Tansu Daylan, Jonathan J. Fortney, Kevin France, Jayesh M. Goyal, David Grant, James Kirk, Laura Kreidberg, Amy Louca, Sarah E. Moran, Sagnick Mukherjee, Evert Nasedkin, Kazumasa Ohno, Benjamin V. Rackham, Seth Redfield, Jake Taylor, Pascal Tremblin, Channon Visscher, Nicole L. Wallack, Luis Welbanks, Allison Youngblood, Eva-Maria Ahrer, Natasha E. Batalha, Patrick Behr, Zachory K. Berta-Thompson, Jasmina Blečić, S. L. Casewell, Ian J. M. Crossfield, Nicolas Crouzet, Patricio E. Cubillos, Leen Decin, Jean-Michel Desert, Adina D. Feinstein, Neale P. Gibson, Joseph Harrington, Kevin Heng, Thomas Henning, Eliza M.-R. Kempton, Jessica Krick, Pierre-Olivier Lagage, Monika Lendl, Joshua D. Lothringer, Megan Mansfield, N. J. Mayne, Thomas Mikal-Evans, Enric Palle, Everett Schlawin, Oliver Shorttle, Peter J. Wheatley, and Sergei N. Yurchenko. Photochemically produced SO₂ in the atmosphere of WASP-39b. *Nature*, 617(7961):483–487, May 2023. ISSN 0028-0836, 1476-4687. doi: 10.1038/s41586-023-05902-2. URL <https://www.nature.com/articles/s41586-023-05902-2>.
- Caroline Dorn and Tim Lichtenberg. Hidden Water in Magma Ocean Exoplanets. *Astrophysical Journal Letters*, 922(1):L4, November 2021. doi: 10.3847/2041-8213/ac33af.
- Oliver Shorttle, Sean Jordan, Harrison Nicholls, Tim Lichtenberg, and Dan J. Bower. Distinguishing oceans of water from magma on mini-neptune k2-18b. *The Astrophysical Journal Letters*, 962(1):L8, feb 2024. doi: 10.3847/2041-8213/ad206e. URL <https://dx.doi.org/10.3847/2041-8213/ad206e>.
- Trevor J. David, Gabriella Contardo, Angeli Sandoval, Ruth Angus, Yuxi (Lucy) Lu, Megan Bedell, Jason L. Curtis, Daniel Foreman-

- Mackey, Benjamin J. Fulton, Samuel K. Grunblatt, and Erik A. Petigura. Evolution of the exoplanet size distribution: Forming large super-earths over billions of years. *The Astronomical Journal*, 161(6):265, may 2021. doi: 10.3847/1538-3881/abf439. URL <https://dx.doi.org/10.3847/1538-3881/abf439>.
- Xuan Ji, Richard D. Chatterjee, Brandon Park Coy, and Edwin S. Kite. The Cosmic Shoreline Revisited: A Metric for Atmospheric Retention Informed by Hydrodynamic Escape. *arXiv e-prints*, art. arXiv:2504.19872, April 2025. doi: 10.48550/arXiv.2504.19872.
- Eliza M. R. Kempton and Heather A. Knutson. Transiting Exoplanet Atmospheres in the Era of JWST. *Reviews in Mineralogy and Geochemistry*, 90(1):411–464, July 2024. doi: 10.2138/rmg.2024.90.12.
- Tim Lichtenberg and Yamila Miguel. Super-Earths and Earth-like Exoplanets. *Treatise on Geochemistry*, 7:51–112, January 2025. doi: 10.1016/B978-0-323-99762-1.00122-4.
- Benjamin J. Fulton and Erik A. Petigura. The California- *Kepler* Survey. VII. Precise Planet Radii Leveraging *Gaia* DR2 Reveal the Stellar Mass Dependence of the Planet Radius Gap. *The Astronomical Journal*, 156(6):264, November 2018. ISSN 1538-3881. doi: 10.3847/1538-3881/aae828. URL <https://iopscience.iop.org/article/10.3847/1538-3881/aae828>.
- James E. Owen. Atmospheric escape and the evolution of close-in exoplanets. *Annual Review of Earth and Planetary Sciences*, 47(Volume 47, 2019):67–90, 2019. ISSN 1545-4495. doi: <https://doi.org/10.1146/annurev-earth-053018-060246>. URL <https://www.annualreviews.org/content/journals/10.1146/annurev-earth-053018-060246>.
- Eric D. Lopez. Born dry in the photoevaporation desert: Kepler’s ultra-short-period planets formed water-poor. *Monthly Notices of the Royal Astronomical Society*, 472(1):245–253, 06 2017. ISSN 0035-8711. doi: 10.1093/mnras/stx1558. URL <https://doi.org/10.1093/mnras/stx1558>.
- Olivier Mousis, Magali Deleuil, Artyom Aguiçhine, Emmanuel Marcq, Joseph Naar, Lorena Acuña Aguirre, Bastien Brugger, and Thomas Gonçalves. Irradiated ocean planets bridge super-earth and sub-neptune populations. *The Astrophysical Journal Letters*, 896(2):L22, jun 2020. doi: 10.3847/2041-8213/ab9530. URL <https://dx.doi.org/10.3847/2041-8213/ab9530>.
- G. Lacedelli, T. G. Wilson, L. Malavolta, M. J. Hooton, A. Collier Cameron, Y. Alibert, A. Mortier, A. Bonfanti, R. D. Haywood, S. Hoyer, G. Piotto, A. Bekkelien, A. M. Vanderburg, W. Benz, X. Dumusque, A. Deline, M. López-Morales, L. Borsato, K. Rice, L. Fossati, D. W. Latham, A. Brandeker, E. Poretti, S. G. Sousa, A. Sozzetti, S. Salmon, C. J. Burke, V. Van Grootel, M. M. Fausnaugh, V. Adibekyan, C. X. Huang, H. P. Osborn, A. J. Mustill, E. Pallé, V. Bourrier, V. Nascimbeni, R. Alonso, G. Anglada, T. Bárczy, D. Barrado y Navascues, S. C. C. Barros, W. Baumjohann, M. Beck, T. Beck, N. Billot, X. Bonfils, C. Broeg, L. A. Buchhave, J. Cabrera, S. Charoz, R. Cosentino, Sz Csizmadia, M. B. Davies, M. Deleuil, L. Delrez, O. Demangeon, B. O. Demory, D. Ehrenreich, A. Erikson, E. Esparza-Borges, H. G. Florén, A. Fortier, M. Fridlund, D. Futyan, D. Gandolfi, A. Ghedina, M. Gillon, M. Güdel, P. Guterman, A. Harutyunyan, K. Heng, K. G. Isaak, J. M. Jenkins, L. Kiss, J. Laskar, A. Lecavelier des Etangs, M. Lendl, C. Lovis, D. Magrin, L. Marafatto, A. F. Martinez Fiorenzano, P. F. L. Maxted, M. Mayor, G. Micela, E. Molinari, F. Murgas, N. Narita, G. Olofsson, R. Ottensamer, I. Pagano, A. Pasetti, M. Pedani, F. A. Pepe, G. Peter, D. F. Phillips, D. Pollacco, D. Queloz, R. Ragazzoni, N. Rando, F. Ratti, H. Rauer, I. Ribas, N. C. Santos, D. Sasselov, G. Scandariato, S. Seager, D. Ségransan, L. M. Serrano, A. E. Simon, A. M. S. Smith, M. Steinberger, M. Steller, Gy Szabó, N. Thomas, J. D. Twicken, S. Udry, N. Walton, and J. N. Winn. Investigating the architecture and internal structure of the TOI-561 system planets with CHEOPS, HARPS-N, and TESS. *Monthly Notices of the Royal Astronomical Society*, 511(3):4551–4571, April 2022. doi: 10.1093/mnras/stac199.
- Rachel B. Fernandes, Galen J. Bergsten, Gijs D. Mulders, Ilaria Pascucci, Kevin K. Hardegree-Ullman, Steven Giacalone, Jessie L. Christiansen, James G. Rogers, Akash Gupta, Rebekah I. Dawson, Tommi T. Koskinen, Kiersten M. Boley, Jason L. Curtis, Katia Cunha, Eric E. Mamajek, Sabina Sagynbayeva, Sakhee S. Bhure, David R. Ciardi, Preethi R. Karpoor, Kyle A. Pearson, Jon K. Zink, and Gregory A. Feiden. Signatures of Atmospheric Mass Loss and Planet Migration in the Time Evolution of Short-period Transiting Exoplanets. *Astronomical Journal*, 169(4):208, April 2025. doi: 10.3847/1538-3881/adb97e.
- O. D. S. Demangeon, M. R. Zapatero Osorio, Y. Alibert, S. C. C. Barros, V. Adibekyan, H. M. Tabernero, A. Antoniadis-Karnavas, J. D. Camacho, A. Suárez Mascareño, M. Oshagh, G. Micela, S. G. Sousa, C. Lovis, F. A. Pepe, R. Rebolo, S. Cristiani, N. C. Santos, R. Allart, C. Allende Prieto, D. Bossini, F. Bouchy, A. Cabral, M. Damasso, P. Di Marcantonio, V. D’Odorico, D. Ehrenreich, J. Faria, P. Figueira, R. Génova Santos, J. Haldemann, N. Hara, J. I. González Hernández, B. Lavie, J. Lillo-Box, G. Lo Curto, C. J. A. P. Martins, D. Mégevand, A. Mehner, P. Molaro, N. J. Nunes, E. Pallé, L. Pasquini, E. Poretti, A. Sozzetti, and S. Udry. Warm terrestrial planet with half the mass of Venus transiting a nearby star. *A&A*, 653:A41, September 2021. doi: 10.1051/0004-6361/202140728.
- Li Zhou, Bo Ma, Yonghao Wang, and Yinan Zhu. Hubble WFC3 Spectroscopy of the Rocky Planet L 98-59 b: No Evidence for a Cloud-free Primordial Atmosphere. *Astronomical Journal*, 164(5):203, November 2022. doi: 10.3847/1538-3881/ac8fe9.
- Aaron Bello-Arufe, Mario Damiano, Katherine A. Bennett, Renyu Hu, Luis Welbanks, Ryan J. MacDonald, Darryl Z. Seligman, David K. Sing, Armen Tokadjian, Apurva Oza, and Jeehyun Yang. Evidence for a volcanic atmosphere on the sub-earth I98-59b, 2025. URL <https://arxiv.org/abs/2501.18680>.
- Li Zhou, Bo Ma, Yong-Hao Wang, and Yi-Nan Zhu. Hubble WFC3 Spectroscopy of the Terrestrial Planets L 98-59 c and d: No Evidence for a Clear Hydrogen Dominated Primary Atmosphere. *Research in Astronomy and Astrophysics*, 23(2):025011, February 2023. doi: 10.1088/1674-4527/acaceb.
- Vinesh M. Rajpaul, Oscar Barragán, and Norbert Zicher. A non-zero Doppler amplitude is not enough: revisiting the putative radial velocity detection of sub-Venus exoplanet L 98-59b. *Monthly Notices of the Royal Astronomical Society*, 530(4):4665–4675, June 2024. doi: 10.1093/mnras/stae778.
- Léna Parc, François Bouchy, Julia Venturini, Caroline Dorn, and Ravit Helled. From super-Earths to sub-Neptunes: Observational constraints and connections to theoretical models. *A&A*, 688:A59, August 2024. doi: 10.1051/0004-6361/202449911.
- Harrison Nicholls, Tim Lichtenberg, Dan J. Bower, and Raymond Pierrehumbert. Magma ocean evolution at arbitrary redox state. *Journal of Geophysical Research: Planets*, 129(12):e2024JE008576, 2024b. doi: <https://doi.org/10.1029/2024JE008576>. URL <https://agupubs.onlinelibrary.wiley.com/doi/abs/10.1029/2024JE008576>. e2024JE008576 2024JE008576.
- Hamish Innes, Shang-Min Tsai, and Raymond T. Pierrehumbert. The Runaway Greenhouse Effect on Hycean Worlds. *Astrophysical Journal*, 953(2):168, August 2023. doi: 10.3847/1538-4357/ace346.
- Owen R. Lehmer and David C. Catling. Rocky worlds limited to 1.8 earth radii by atmospheric escape during a star’s extreme uv saturation. *The Astrophysical Journal*, 845(2):130, aug 2017. doi: 10.3847/1538-4357/aa8137. URL <https://dx.doi.org/10.3847/1538-4357/aa8137>.
- Julia Venturini, Octavio M. Guilera, Jonas Haldemann, María P. Ronco, and Christoph Mordasini. The nature of the radius valley. Hints from formation and evolution models. *A&A*, 643:L1, November 2020. doi: 10.1051/0004-6361/202039141.
- Hilke E. Schlichting and Edward D. Young. Chemical equilibrium between Cores, Mantles, and Atmospheres of Super-Earths and Sub-Neptunes, and Implications for their Compositions, Interiors and Evolution, March 2022. URL <http://arxiv.org/abs/2107.10405>. arXiv:2107.10405 [astro-ph].

- Fabrice Gaillard, Fabien Bernadou, Mathieu Roskosz, Mohamed Ali Bouhifd, Yves Marrochi, Giada Iacono-Marziano, Manuel Moreira, Bruno Scaillet, and Gregory Rogerie. Redox controls during magma ocean degassing. *Earth and Planetary Science Letters*, 577:117255, 2022. ISSN 0012-821X. doi: <https://doi.org/10.1016/j.epsl.2021.117255>. URL <https://www.sciencedirect.com/science/article/pii/S0012821X21005112>.
- Joshua Krissansen-Totton, Nicholas Wogan, Maggie Thompson, and Jonathan J. Fortney. The erosion of large primary atmospheres typically leaves behind substantial secondary atmospheres on temperate rocky planets. *Nature Communications*, 15(1):8374, Sep 2024. ISSN 2041-1723. doi: [10.1038/s41467-024-52642-6](https://doi.org/10.1038/s41467-024-52642-6). URL <https://doi.org/10.1038/s41467-024-52642-6>.
- S. Krijt, M. Kama, M. McClure, J. Teske, E. A. Bergin, O. Shorttle, K. J. Walsh, and S. N. Raymond. Chemical Habitability: Supply and Retention of Life’s Essential Elements During Planet Formation. In S. Inutsuka, Y. Aikawa, T. Muto, K. Tomida, and M. Tamura, editors, *Protostars and Planets VII*, volume 534 of *Astronomical Society of the Pacific Conference Series*, page 1031, July 2023. doi: [10.48550/arXiv.2203.10056](https://arxiv.org/abs/2203.10056).
- Cynthia S K Ho, James G Rogers, Vincent van Eylen, James E Owen, and Hilke E Schlichting. Shallower radius valley around low-mass hosts: evidence for icy planets, collisions, or high-energy radiation scatter. *Monthly Notices of the Royal Astronomical Society*, 531(3):3698–3714, 05 2024. ISSN 0035-8711. doi: [10.1093/mnras/stae1376](https://doi.org/10.1093/mnras/stae1376). URL <https://doi.org/10.1093/mnras/stae1376>.
- Antonio Costa, Luca Caricchi, and Nikolai Bagdassarov. A model for the rheology of particle-bearing suspensions and partially molten rocks. *Geochemistry, Geophysics, Geosystems*, 10(3), 2009. doi: <https://doi.org/10.1029/2008GC002138>. URL <https://agupubs.onlinelibrary.wiley.com/doi/abs/10.1029/2008GC002138>.
- Olivier Namur, Bernard Charlier, Francois Holtz, Camille Cartier, and Catherine McCammon. Sulfur solubility in reduced mafic silicate melts: Implications for the speciation and distribution of sulfur on mercury. *Earth and Planetary Science Letters*, 448: 102–114, 2016. ISSN 0012-821X. doi: <https://doi.org/10.1016/j.epsl.2016.05.024>. URL <https://www.sciencedirect.com/science/article/pii/S0012821X16302412>.
- Daria Kubyshkina, Aline A Vidotto, Luca Fossati, and Eoin Farrell. Coupling thermal evolution of planets and hydrodynamic atmospheric escape in mesa. *Monthly Notices of the Royal Astronomical Society*, 499(1):77–88, 09 2020. ISSN 0035-8711. doi: [10.1093/mnras/staa2815](https://doi.org/10.1093/mnras/staa2815). URL <https://doi.org/10.1093/mnras/staa2815>.
- Eric D. Lopez and Jonathan J. Fortney. Understanding the mass–radius relation for sub-neptunes: Radius as a proxy for composition. *The Astrophysical Journal*, 792(1):1, aug 2014. doi: [10.1088/0004-637X/792/1/1](https://doi.org/10.1088/0004-637X/792/1/1). URL <https://dx.doi.org/10.1088/0004-637X/792/1/1>.
- Diana Powell, Adina D. Feinstein, Elspeth K. H. Lee, Michael Zhang, Shang-Min Tsai, Jake Taylor, James Kirk, Taylor Bell, Joanna K. Barstow, Peter Gao, Jacob L. Bean, Jasmina Blečić, Katy L. Chubb, Ian J. M. Crossfield, Sean Jordan, Daniel Kitzmann, Sarah E. Moran, Giuseppe Morello, Julianne I. Moses, Luis Welbanks, Jeehyun Yang, Xi Zhang, Eva-Maria Ahrer, Aaron Bello-Arufe, Jonathan Brande, S. L. Casewell, Nicolas Crouzet, Patricio E. Cubillos, Brice-Olivier Demory, Achrène Dyrek, Laura Flagg, Renyu Hu, Julie Inglis, Kathryn D. Jones, Laura Kreidberg, Mercedes López-Morales, Pierre-Olivier Lagage, Erik A. Meier Valdés, Yamila Miguel, Vivien Parmentier, Anjali A. A. Piette, Benjamin V. Rackham, Michael Radica, Seth Redfield, Kevin B. Stevenson, Hannah R. Wakeford, Keshav Aggarwal, Munazza K. Alam, Natalie M. Batalha, Natasha E. Batalha, Björn Benneke, Zach K. Berta-Thompson, Ryan P. Brady, Claudio Caceres, Aarynn L. Carter, Jean-Michel Désert, Joseph Harrington, Nicolas Iro, Michael R. Line, Joshua D. Lothringer, Ryan J. MacDonald, Luigi Mancini, Karan Molaverdikhani, Sagnick Mukherjee, Matthew C. Nixon, Apurva V. Oza, Enric Palle, Zafar Rustamkulov, David K. Sing, Maria E. Steinrueck, Olivia Venot, Peter J. Wheatley, and Sergei N. Yurchenko. Sulfur dioxide in the mid-infrared transmission spectrum of wasp-39b. *Nature*, 626(8001):979–983, Feb 2024. ISSN 1476-4687. doi: [10.1038/s41586-024-07040-9](https://doi.org/10.1038/s41586-024-07040-9). URL <https://doi.org/10.1038/s41586-024-07040-9>.
- Edwin S. Kite, Bruce Fegley Jr., Laura Schaefer, and Eric Gaidos. Atmosphere-interior exchange on hot, rocky exoplanets. *The Astrophysical Journal*, 828(2):80, sep 2016. doi: [10.3847/0004-637X/828/2/80](https://doi.org/10.3847/0004-637X/828/2/80). URL <https://dx.doi.org/10.3847/0004-637X/828/2/80>.
- Edwin S. Kite and Megan N. Barnett. Exoplanet secondary atmosphere loss and revival. *Proceedings of the National Academy of Sciences*, 117(31):18264–18271, August 2020. ISSN 0027-8424, 1091-6490. doi: [10.1073/pnas.2006177117](https://doi.org/10.1073/pnas.2006177117). URL <https://pnas.org/doi/full/10.1073/pnas.2006177117>.
- Palle, E., Orell-Miquel, J., Brady, M., Bean, J., Hatzes, A. P., Morello, G., Morales, J. C., Murgas, F., Molaverdikhani, K., Parviainen, H., Sanz-Forcada, J., Bejar, V. J. S., Caballero, J. A., Sreenivas, K. R., Schlecker, M., Ribas, I., Perdelwitz, V., Tal-Or, L., Perez-Torres, M., Luque, R., Dreizler, S., Fuhrmeister, B., Aceituno, F., Amado, P. J., Anglada-Escude, G., Caldwell, D. A., Charbonneau, D., Cifuentes, C., de Leon, J. P., Collins, K. A., Dufoer, S., Espinoza, N., Essack, Z., Fukui, A., Chew, Y. Gomez Maqueo, Gomez-Muñoz, M. A., Henning, Th., Herrero, E., Jeffers, S.V., Jenkins, J., Kaminski, A., Kasper, J., Kunimoto, M., Latham, D., Lillo-Box, J., Lopez-Gonzalez, M. J., Montes, D., Mori, M., Narita, N., Quirrenbach, A., Pedraz, S., Reiners, A., Rodríguez, E., Rodríguez-Lopez, C., Sabin, L., Schanche, N., Schwarz, R.-P., Schweitzer, A., Seifahrt, A., Stefansson, G., Sturmer, J., Trifonov, T., Vanaverbeke, S., Wells, R. D., Zapatero-Osorio, M. R., and Zechmeister, M. GJ 806 (toi-4481): A bright nearby multi-planetary system with a transiting hot low-density super-earth. *A&A*, 678:A80, 2023. doi: [10.1051/0004-6361/202244261](https://doi.org/10.1051/0004-6361/202244261). URL <https://doi.org/10.1051/0004-6361/202244261>.
- Dan J. Bower, Patrick Sanan, and Aaron S. Wolf. Numerical solution of a non-linear conservation law applicable to the interior dynamics of partially molten planets. *Physics of the Earth and Planetary Interiors*, 274:49–62, January 2018. ISSN 00319201. doi: [10.1016/j.pepi.2017.11.004](https://doi.org/10.1016/j.pepi.2017.11.004). URL <https://linkinghub.elsevier.com/retrieve/pii/S0031920117302042>.
- Dan J. Bower, Kaustubh Hakim, Paolo A. Sossi, and Patrick Sanan. Retention of Water in Terrestrial Magma Oceans and Carbon-rich Early Atmospheres. *The Planetary Science Journal*, 3(4):93, April 2022. ISSN 2632-3338. doi: [10.3847/PSJ/ac5fb1](https://doi.org/10.3847/PSJ/ac5fb1). URL <https://iopscience.iop.org/article/10.3847/PSJ/ac5fb1>.
- Harrison Nicholls, Raymond Pierrehumbert, and Tim Lichtenberg. Agni: A radiative-convective model for lava planet atmospheres. *Journal of Open Source Software*, 10(109):7726, 2025b. doi: [10.21105/joss.07726](https://doi.org/10.21105/joss.07726). URL <https://doi.org/10.21105/joss.07726>.
- Paolo A. Sossi, Peter M. E. Tollan, James Badro, and Dan J. Bower. Solubility of water in peridotite liquids and the prevalence of steam atmospheres on rocky planets. *Earth and Planetary Science Letters*, 601:117894, January 2023. ISSN 0012-821X. doi: [10.1016/j.epsl.2022.117894](https://doi.org/10.1016/j.epsl.2022.117894).
- Hamish C. F. C. Hay, Antony Trinh, and Isamu Matsuyama. Powering the Galilean Satellites with Moon-Moon Tides. *Geophysical Research Letters*, 47(15):e88317, August 2020. doi: [10.1029/2020GL088317](https://doi.org/10.1029/2020GL088317).
- Keiko Hamano, Hajime Kawahara, Yutaka Abe, Masanori Onishi, and George L. Hashimoto. LIFETIME AND SPECTRAL EVOLUTION OF A MAGMA OCEAN WITH A STEAM ATMOSPHERE: ITS DETECTABILITY BY FUTURE DIRECT IMAGING. *The Astrophysical Journal*, 806(2):216, June 2015. ISSN 1538-4357. doi: [10.1088/0004-637X/806/2/216](https://doi.org/10.1088/0004-637X/806/2/216). URL <https://iopscience.iop.org/article/10.1088/0004-637X/806/2/216>.
- Laura Schaefer, Robin D. Wordsworth, Zachory Berta-Thompson, and Dimitar Sasselov. Predictions of the atmospheric composition of GJ 1132b. *The Astrophysical Journal*, 829(2):63, sep 2016. doi:

- 10.3847/0004-637X/829/2/63. URL <https://dx.doi.org/10.3847/0004-637X/829/2/63>.
- Adam M. Dziewonski and Don L. Anderson. Preliminary reference earth model. *Physics of the Earth and Planetary Interiors*, 25(4):297–356, 1981. ISSN 0031-9201. doi: [https://doi.org/10.1016/0031-9201\(81\)90046-7](https://doi.org/10.1016/0031-9201(81)90046-7). URL <https://www.sciencedirect.com/science/article/pii/0031920181900467>.
- Haiyang Luo, Caroline Dorn, and Jie Deng. The interior as the dominant water reservoir in super-earths and sub-neptunes. *Nature Astronomy*, 8(11):1399–1407, Nov 2024. ISSN 2397-3366. doi: [10.1038/s41550-024-02347-z](https://doi.org/10.1038/s41550-024-02347-z). URL <https://doi.org/10.1038/s41550-024-02347-z>.
- Kei Hirose, Bernard Wood, and Lidunka Vočadlo. Light elements in the earth’s core. *Nature Reviews Earth & Environment*, 2(9):645–658, Sep 2021. ISSN 2662-138X. doi: [10.1038/s43017-021-00203-6](https://doi.org/10.1038/s43017-021-00203-6). URL <https://doi.org/10.1038/s43017-021-00203-6>.
- Dan J. Bower, Daniel Kitzmann, Aaron S. Wolf, Patrick Sanan, Caroline Dorn, and Apurva V. Oza. Linking the evolution of terrestrial interiors and an early outgassed atmosphere to astrophysical observations. *Astronomy & Astrophysics*, 631:A103, November 2019. ISSN 0004-6361, 1432-0746. doi: [10.1051/0004-6361/201935710](https://doi.org/10.1051/0004-6361/201935710). URL <https://www.aanda.org/10.1051/0004-6361/201935710>.
- Aaron S. Wolf and Dan J. Bower. An equation of state for high pressure-temperature liquids (rtpress) with application to mg-sio3 melt. *Physics of the Earth and Planetary Interiors*, 278:59–74, 2018. ISSN 0031-9201. doi: <https://doi.org/10.1016/j.pepi.2018.02.004>. URL <https://www.sciencedirect.com/science/article/pii/S0031920117301449>.
- Katharina Lodders and Bruce Fegley. *The planetary scientist’s companion / Katharina Lodders, Bruce Fegley*. 1998.
- Kiersten M. Boley, Wendy R. Panero, Cayman T. Unterborn, Joseph G. Schulze, Romy Rodriguez Martinez, and Ji Wang. Fizzy Super-Earths: Impacts of Magma Composition on the Bulk Density and Structure of Lava Worlds. 2023. doi: [10.48550/ARXIV.2307.13726](https://arxiv.org/abs/2307.13726). URL <https://arxiv.org/abs/2307.13726>. Publisher: arXiv Version Number: 1.
- C. T. Unterborn and W. R. Panero. The pressure and temperature limits of likely rocky exoplanets. *Journal of Geophysical Research: Planets*, 124(7):1704–1716, 2019. doi: <https://doi.org/10.1029/2018JE005844>. URL <https://agupubs.onlinelibrary.wiley.com/doi/abs/10.1029/2018JE005844>.
- J. M. Edwards and A. Slingo. Studies with a flexible new radiation code. I: Choosing a configuration for a large-scale model. *Quarterly Journal of the Royal Meteorological Society*, 122(531):689–719, April 1996. ISSN 00359009, 1477870X. doi: [10.1002/qj.49712253107](https://doi.org/10.1002/qj.49712253107). URL <https://onlinelibrary.wiley.com/doi/10.1002/qj.49712253107>.
- David Amundsen, Isabelle Baraffe, Pascal Tremblin, James Manners, Wolfgang Hayek, Nathan Mayne, and David Acreman. Accuracy tests of radiation schemes used in hot Jupiter global circulation models. *A&A*, 564:A59, 2014. doi: [10.1051/0004-6361/201323169](https://doi.org/10.1051/0004-6361/201323169). URL <https://doi.org/10.1051/0004-6361/201323169>.
- Meridith Joyce and Jamie Tayar. A Review of the Mixing Length Theory of Convection in 1D Stellar Modeling. *Galaxies*, 11(3):75, June 2023. ISSN 2075-4434. doi: [10.3390/galaxies11030075](https://doi.org/10.3390/galaxies11030075). URL <https://www.mdpi.com/2075-4434/11/3/75>.
- C. P. Johnstone, M. Bartel, and M. Gudel. The active lives of stars: A complete description of the rotation and XUV evolution of F, G, K, and M dwarfs. *Astronomy & Astrophysics*, 649:A96, May 2021. ISSN 0004-6361, 1432-0746. doi: [10.1051/0004-6361/202038407](https://doi.org/10.1051/0004-6361/202038407). URL <https://www.aanda.org/10.1051/0004-6361/202038407>.
- Scott G. Engle and Edward F. Guinan. Living with a red dwarf: The rotation–age relationships of m dwarfs. *The Astrophysical Journal Letters*, 954(2):L50, sep 2023. doi: [10.3847/2041-8213/acf472](https://doi.org/10.3847/2041-8213/acf472). URL <https://dx.doi.org/10.3847/2041-8213/acf472>.
- Patrick R. Behr, Kevin France, Alexander Brown, Girish Duvvuri, Jacob L. Bean, Zachory Berta-Thompson, Cynthia Froning, Yamila Miguel, J. Sebastian Pineda, David J. Wilson, and Allison Youngblood. The MUSCLES Extension for Atmospheric Transmission Spectroscopy: UV and X-Ray Host-star Observations for JWST ERS & GTO Targets. *Astronomical Journal*, 166(1):35, July 2023. doi: [10.3847/1538-3881/acdb70](https://doi.org/10.3847/1538-3881/acdb70).
- Yao Tang, Jonathan J. Fortney, and Ruth Murray-Clay. Assessing core-powered mass loss in the context of early boil-off: Minimal long-lived mass loss for the sub-neptune population. *The Astrophysical Journal*, 976(2):221, nov 2024. doi: [10.3847/1538-4357/ad8567](https://doi.org/10.3847/1538-4357/ad8567). URL <https://dx.doi.org/10.3847/1538-4357/ad8567>.
- Tim Lichtenberg, Laura K. Schaefer, Miki Nakajima, and Rebecca A. Fischer. Geophysical Evolution During Rocky Planet Formation. In S. Inutsuka, Y. Aikawa, T. Muto, K. Tomida, and M. Tamura, editors, *Protostars and Planets VII*, volume 534 of *Astronomical Society of the Pacific Conference Series*, page 907, July 2023. doi: [10.48550/arXiv.2203.10023](https://doi.org/10.48550/arXiv.2203.10023).
- Saswata Hier-Majumder and Marc M. Hirschmann. The origin of volatiles in the earth’s mantle. *Geochemistry, Geophysics, Geosystems*, 18(8):3078–3092, 2017. doi: <https://doi.org/10.1002/2017GC006937>. URL <https://agupubs.onlinelibrary.wiley.com/doi/abs/10.1002/2017GC006937>.
- Shi J. Sim, Marc M. Hirschmann, and Saswata Hier-Majumder. Volatile and trace element storage in a crystallizing martian magma ocean. *Journal of Geophysical Research: Planets*, 129(8):e2024JE008346, 2024. doi: <https://doi.org/10.1029/2024JE008346>. URL <https://agupubs.onlinelibrary.wiley.com/doi/abs/10.1029/2024JE008346>. e2024JE008346 2024JE008346.
- Philippa Liggins, Sean Jordan, Paul B. Rimmer, and Oliver Shorttle. Growth and Evolution of Secondary Volcanic Atmospheres: I. Identifying the Geological Character of Hot Rocky Planets. *Journal of Geophysical Research: Planets*, 127(7), July 2022. ISSN 2169-9097, 2169-9100. doi: [10.1029/2021JE007123](https://doi.org/10.1029/2021JE007123). URL <https://onlinelibrary.wiley.com/doi/10.1029/2021JE007123>.
- F. Gaillard, M. A. Bouhifd, E. Furi, V. Malavergne, Y. Marrochi, L. Noack, G. Ortenzi, M. Roskosz, and S. Vulpis. The Diverse Planetary Ingassing/Outgassing Paths Produced over Billions of Years of Magmatic Activity. *Space Science Reviews*, 217(1):22, February 2021. ISSN 0038-6308, 1572-9672. doi: [10.1007/s11214-021-00802-1](https://doi.org/10.1007/s11214-021-00802-1). URL <https://link.springer.com/10.1007/s11214-021-00802-1>.
- C. P. Johnstone. Hydrodynamic escape of water vapor atmospheres near very active stars. *ApJ*, 890(1):79, feb 2020. doi: [10.3847/1538-4357/ab6224](https://doi.org/10.3847/1538-4357/ab6224). URL <https://dx.doi.org/10.3847/1538-4357/ab6224>.
- Tatsuya Yoshida, Naoki Terada, and Kiyoshi Kuramoto. Suppression of hydrodynamic escape of an h2-rich early earth atmosphere by radiative cooling of carbon oxides. *Progress in Earth and Planetary Science*, 11(1):59, Nov 2024. ISSN 2197-4284. doi: [10.1186/s40645-024-00666-3](https://doi.org/10.1186/s40645-024-00666-3). URL <https://doi.org/10.1186/s40645-024-00666-3>.
- R. Cloutier, N. Astudillo-Defru, X. Bonfils, J. S. Jenkins, Z. Berdiñas, G. Ricker, R. Vanderspek, D. W. Latham, S. Seager, J. Winn, J. M. Jenkins, J. M. Almenara, F. Bouchy, X. Delfosse, M. R. Díaz, R. F. Díaz, R. Doyon, P. Figueira, T. Forveille, N. T. Kurtovic, C. Lovis, M. Mayor, K. Menou, E. Morgan, R. Morris, P. Muirhead, F. Murgas, F. Pepe, N. C. Santos, D. Ségransan, J. C. Smith, P. Tenenbaum, G. Torres, S. Udry, M. Vezie, and J. Villaseñor. Characterization of the L 98-59 multi-planetary system with HARPS. Mass characterization of a hot super-Earth, a sub-Neptune, and a mass upper limit on the third planet. *A&A*, 629:A111, September 2019. doi: [10.1051/0004-6361/201935957](https://doi.org/10.1051/0004-6361/201935957).
- James G. Rogers. On the road to the radius valley: distinguishing between gas dwarfs and water worlds with young transiting exoplanets. *arXiv e-prints*, art. arXiv:2503.17364, March 2025. doi: [10.48550/arXiv.2503.17364](https://doi.org/10.48550/arXiv.2503.17364).

- Collin Cherubim, Robin Wordsworth, Dan Bower, Paolo Sossi, Danica Adams, and Renyu Hu. An Oxidation Gradient Straddling the Small Planet Radius Valley. *arXiv e-prints*, art. arXiv:2503.05055, March 2025. doi: 10.48550/arXiv.2503.05055.
- R. D. Wordsworth and R. T. Pierrehumbert. Water loss from terrestrial planets with co₂-rich atmospheres. *The Astrophysical Journal*, 778(2):154, nov 2013. doi: 10.1088/0004-637X/778/2/154. URL <https://dx.doi.org/10.1088/0004-637X/778/2/154>.
- Leslie A. Rogers. Most 1.6 Earth-radius planets are not rocky. *The Astrophysical Journal*, 801(1):41, March 2015. ISSN 0004-637X. doi: 10.1088/0004-637X/801/1/41.
- Franck Selsis, Jeremy Leconte, Martin Turbet, Guillaume Chaverot, and emeline Bolmont. A cool runaway greenhouse without surface magma ocean. *Nature*, 620(7973):287–291, August 2023. ISSN 0028-0836, 1476-4687. doi: 10.1038/s41586-023-06258-3. URL <https://www.nature.com/articles/s41586-023-06258-3>.
- Ben Dorman, Alan W. Irwin, and Brian B. Pedersen. On Equation of State Interpolation Errors in Stellar Interior Calculations. *Astrophysical Journal*, 381:228, November 1991. doi: 10.1086/170644.
- D. Saumon, G. Chabrier, and H. M. van Horn. An Equation of State for Low-Mass Stars and Giant Planets. *Astrophysical Journal Supplement*, 99:713, August 1995. doi: 10.1086/192204.
- Isabelle Baraffe, Derek Homeier, France Allard, and Gilles Chabrier. New evolutionary models for pre-main sequence and main sequence low-mass stars down to the hydrogen-burning limit. *Astronomy & Astrophysics*, 577:A42, May 2015. ISSN 0004-6361, 1432-0746. doi: 10.1051/0004-6361/201425481. URL <http://www.aanda.org/10.1051/0004-6361/201425481>.
- B. Paxton, L. Bildsten, A. Dotter, F. Herwig, P. Lesaffre, and F. Timmes. Modules for Experiments in Stellar Astrophysics (MESA). *Astrophysical Journal Supplement*, 192:3, jan 2011. doi: 10.1088/0067-0049/192/1/3.
- R J Magyar, S Root, and T R Mattsson. Equations of state for mixtures: results from density-functional (dft) simulations compared to high accuracy validation experiments on z. *Journal of Physics: Conference Series*, 500(16):162004, may 2014. doi: 10.1088/1742-6596/500/16/162004. URL <https://dx.doi.org/10.1088/1742-6596/500/16/162004>.
- Rudolph J. Magyar, Seth Root, Kyle Cochrane, Thomas R. Mattsson, and Dawn G. Flicker. Ethane-xenon mixtures under shock conditions. *Phys. Rev. B*, 91:134109, Apr 2015. doi: 10.1103/PhysRevB.91.134109. URL <https://link.aps.org/doi/10.1103/PhysRevB.91.134109>.
- P. A. Bradley, E. N. Loomis, E. C. Merritt, J. A. Guzik, P. H. Denne, and T. T. Clark. Experimental validation of thermodynamic mixture rules at extreme pressures and densities. *Physics of Plasmas*, 25(1):012710, 01 2018. ISSN 1070-664X. doi: 10.1063/1.5006200. URL <https://doi.org/10.1063/1.5006200>.
- Jonas Haldemann, Yann Alibert, Christoph Mordasini, and Willy Benz. Aqua: a collection of h₂o equations of state for planetary models. *A&A*, 643:A105, 2020. doi: 10.1051/0004-6361/202038367. URL <https://doi.org/10.1051/0004-6361/202038367>.
- G. Chabrier, S. Mazevet, and F. Soubiran. A new equation of state for dense hydrogen–helium mixtures. *The Astrophysical Journal*, 872(1):51, feb 2019. doi: 10.3847/1538-4357/aaf99f. URL <https://dx.doi.org/10.3847/1538-4357/aaf99f>.
- Nikku Madhusudhan, Subhjit Sarkar, Savvas Constantinou, Måns Holmberg, Anjali Piette, and Julianne I. Moses. Carbon-bearing Molecules in a Possible Hycean Atmosphere, September 2023. URL <http://arxiv.org/abs/2309.05566>. arXiv:2309.05566 null.
- Haiyang S. Wang, Charles H. Lineweaver, and Trevor R. Ireland. The elemental abundances (with uncertainties) of the most earth-like planet. *Icarus*, 299:460–474, 2018. ISSN 0019-1035. doi: <https://doi.org/10.1016/j.icarus.2017.08.024>. URL <https://www.sciencedirect.com/science/article/pii/S0019103517302221>.
- Dustin Trail, E. Bruce Watson, and Nicholas D. Tailby. The oxidation state of hadean magmas and implications for early earth’s atmosphere. *Nature*, 480(7375):79–82, Dec 2011. ISSN 1476-4687. doi: 10.1038/nature10655. URL <https://doi.org/10.1038/nature10655>.
- Catherine McCammon. Perovskite as a possible sink for ferric iron in the lower mantle. *Nature*, 387(6634):694–696, June 1997. ISSN 1476-4687. doi: 10.1038/42685.
- J. Wade and B. J. Wood. Core formation and the oxidation state of the Earth. *Earth and Planetary Science Letters*, 236(1):78–95, July 2005. ISSN 0012-821X. doi: 10.1016/j.epsl.2005.05.017.
- Jonathan P. Itcovitz, Auriol S. P. Rae, Robert I. Citron, Sarah T. Stewart, Catriona A. Sinclair, Paul B. Rimmer, and Oliver Shorttle. Reduced Atmospheres of Post-impact Worlds: The Early Earth. *The Planetary Science Journal*, 3:115, May 2022. ISSN 2632-3338. doi: 10.3847/PSJ/ac67a9.
- Edwin S. Kite and Laura Schaefer. Water on Hot Rocky Exoplanets. *The Astrophysical Journal Letters*, 909(2):L22, March 2021. ISSN 2041-8205, 2041-8213. doi: 10.3847/2041-8213/abe7dc. URL <https://iopscience.iop.org/article/10.3847/2041-8213/abe7dc>.
- Tim Lichtenberg. Redox Hysteresis of Super-Earth Exoplanets from Magma Ocean Circulation. *The Astrophysical Journal Letters*, 914(1):L4, June 2021. ISSN 2041-8205, 2041-8213. doi: 10.3847/2041-8213/ac0146. URL <https://iopscience.iop.org/article/10.3847/2041-8213/ac0146>.
- Laura Schaefer, Kaveh Pahlevan, and Linda T. Elkins-Tanton. Ferric Iron Evolution During Crystallization of the Earth and Mars. *Journal of Geophysical Research (Planets)*, 129(9):e2023JE008262, September 2024. doi: 10.1029/2023JE008262.10.22541/essoar.170542269. 92961485/v1.
- Robert W. Nicklas, Igor S. Puchtel, and Richard D. Ash. Redox state of the archean mantle: Evidence from v partitioning in 3.5–2.4 ga komatiites. *Geochimica et Cosmochimica Acta*, 222:447–466, 2018. ISSN 0016-7037. doi: <https://doi.org/10.1016/j.gca.2017.11.002>. URL <https://www.sciencedirect.com/science/article/pii/S0016703717307111>.
- D. M. Jorge, I. E. E. Kamp, L. B. F. M. Waters, P. Woitke, and R. J. Spaargaren. Forming planets around stars with non-solar elemental composition. *A&A*, 660:A85, 2022. doi: 10.1051/0004-6361/202142738. URL <https://doi.org/10.1051/0004-6361/202142738>.
- Mark Oosterloo, Inga Kamp, and Wim van Westrenen. The effects of transport processes on the bulk composition of the first generation of planetesimals interior to the water iceline, 2025. URL <https://arxiv.org/abs/2504.15982>.
- P.E. Driscoll and R. Barnes. Tidal heating of earth-like exoplanets around m stars: Thermal, magnetic, and orbital evolutions. *Astrobology*, 15(9):739–760, 2015. doi: 10.1089/ast.2015.1325. URL <https://doi.org/10.1089/ast.2015.1325>. PMID: 26393398.
- G. Gronoff, P. Arras, S. Baraka, J. M. Bell, G. Cessateur, O. Cohen, S. M. Curry, J. J. Drake, M. Elrod, J. Erwin, K. Garcia-Sage, C. Garraffo, A. Glocer, N. G. Heavens, K. Lovato, R. Maggiolo, C. D. Parkinson, C. Simon Wedlund, D. R. Weimer, and W. B. Moore. Atmospheric escape processes and planetary atmospheric evolution. *Journal of Geophysical Research: Space Physics*, 125(8):e2019JA027639, 2020. doi: <https://doi.org/10.1029/2019JA027639>. URL <https://agupubs.onlinelibrary.wiley.com/doi/abs/10.1029/2019JA027639>.